

1 **Scale matters: The influence of structural inheritance on fracture patterns**

2 Anindita Samsu¹, Alexander R. Cruden¹, Steven Micklethwaite¹, Lachlan Grose¹, Stefan A. Vollgger¹

3 ¹*School of Earth, Atmosphere and Environment, Monash University, Clayton, VIC 3800, Australia*

4

5

6

7

8

9 This manuscript is a pre-print and has been accepted for publication in
10 Journal of Structural Geology.

11

12 **Scale matters: The influence of structural inheritance on fracture patterns**

13 Anindita Samsu^{1*}, Alexander R. Cruden¹, Steven Micklethwaite¹, Lachlan Grose¹, Stefan A.

14 Vollgger¹

15 ¹School of Earth, Atmosphere and Environment, Monash University, Clayton, VIC 3800,

16 Australia

17

18 *Corresponding author: anindita.samsu@monash.edu

19

20 Keywords: fractures, faults, structural inheritance, rift basin, Gippsland Basin

21

22 **ABSTRACT**

23 Fracture systems are often geometrically invariant across a range of scales, but the impact of

24 structural inheritance on this relationship is poorly understood. This paper shows how

25 fracture orientations in sedimentary rocks vary at different scales when influenced by pre-rift

26 basement structures. We use high-resolution unmanned aerial vehicle (UAV) orthophotos to

27 map folds and fractures in the basement and cover rocks of the Gippsland Basin, southeast

28 Australia. Outcrop-scale observations are compared with >1 km long faults previously

29 interpreted from potential field data. We use length-coloured rose diagrams of fracture traces

30 to compare trends in fracture orientations. Early Cretaceous syn-rift normal faults exhibit the

31 same ENE-WSW trend at basin (>1 km) and outcrop (meters) scales. Pervasive outcrop-

32 scale, subvertical, NNW-SSE striking joints record a subsequent regional shortening event,

33 but at the basin scale this is only expressed as reverse reactivated ENE-WSW striking faults.

34 Thus, fabrics and/or faults in the underlying basement exert significant control on the

35 orientation of basin-scale fractures in the cover but appear to have limited influence on
36 outcrop-scale fracture orientations. Our observations show that fracture systems influenced
37 by structural inheritance are not scale-invariant, and that a proper understanding of structural
38 architecture can only be achieved by analysing data that span multiple scales.

39 **1. INTRODUCTION**

40 Structural inheritance can impact the location, shape, and orientation of entire rift systems
41 (i.e., tectonic inheritance) (Wilson, 1966; Tommasi and Vauchez, 2001; Thomas, 2006;
42 Manatschal et al., 2015; Schiffer et al., 2018; Heron et al., 2019) as well as smaller-scale
43 faults within rift basins (e.g., Corti et al., 2007; Henza et al., 2011; Reeve et al., 2015; Phillips
44 et al., 2018). Mechanical heterogeneities in pre-rift “basement” rocks can interact with far-
45 field stress during the formation and evolution of a rift basin, influencing fracturing
46 (including faulting) in the sedimentary “cover” rocks. At the scale of an individual basin, one
47 form of interaction between the basement and cover is the reactivation of basement faults and
48 shear zones (McCaffrey, 1997; Holdsworth et al., 2001; Kirkpatrick et al., 2013; Phillips et
49 al., 2016). The presence of such weakened zones in the crust results in a competition between
50 the nucleation of new fractures and failure along a pre-existing zone with a lower shear
51 strength under a particular stress field (Byerlee, 1978; Sibson, 1985). Reactivation may then
52 lead to the formation faults in the cover that are parallel to the pre-existing structure
53 (Holdsworth et al., 1997) and oblique to their expected orientation under an inferred paleo-
54 extension direction (e.g., Corti et al., 2007).

55 Another form of structural inheritance is recognised when the trend of fracture traces in the
56 cover appear to change across areas that overlie different basement domains, even when the
57 fractures do not directly link into the basement structures (Wilson et al., 2010; Samsu et al.,
58 2019). The mechanism behind these variable fracture orientations is unclear but may be the

59 result of local stress perturbations in the vicinity of pre-existing structures, which alter stress
60 trajectories (Bourne and Willemse, 2001; Maerten et al., 2002; de Jossineau et al., 2003;
61 Morley, 2010) and are reflected by a local rotation of the strain axes. Nevertheless, this
62 second, poorly understood mechanism of inheritance can have a significant impact on
63 fracture orientations and connectivity.

64 Few studies examine the influence of inheritance on the formation of fractures in one study
65 area at multiple scales. In a study of the northeast Brazilian margin, Kirkpatrick et al. (2013)
66 found that the orientation of regional rift faults are parallel to sub-vertical, crustal-scale shear
67 zones in the basement, while syn-rift outcrop-scale faults are oblique to the shear zones and
68 the pervasive basement fabric. Their findings suggest that the influence of pre-existing
69 basement structures is scale-dependent. However, it is rarely the case that structures in
70 basement rocks can be compared with the overlying cover rocks at the same scale. The
71 interpretation of faults in cover rocks is usually conducted on seismic reflection data (e.g.,
72 Peace et al., 2018; Phillips et al., 2016; Reeve et al., 2015), while basement structures at the
73 margins of rift basins are observed in outcrops (e.g., Wilson et al., 2006; Kirkpatrick et al.,
74 2013).

75 Our study uses the Cretaceous western onshore Gippsland Basin (southeast Australia; Fig. 1)
76 as a natural laboratory to investigate how pre-existing discrete faults and a pervasive fabric in
77 the basement may have influenced fracture orientations in the overlying cover rocks. Here,
78 we define the basement as any rock unit below the overlying cover. The onshore Gippsland
79 Basin provides a unique opportunity to study the various scales at which inheritance operates.
80 Firstly, the two known levels of basement underneath the basin – a Paleozoic basement and
81 its underlying Neoproterozoic-Cambrian basement – allow us to study multiple orders of
82 inherited structures. Secondly, onshore exposure of basement and cover rocks along the coast
83 allow us to directly compare structures in basement and cover rocks at the same scale.

84

<Insert Figure 1 here>

85 We used high-resolution unmanned aerial vehicle (UAV) orthophotos of outcrops to map pre-
86 existing structures in the basement and thousands of fractures in the cover rocks. Maps of
87 fracture traces (including faults and joints) and orientation statistics of fracture data were
88 used to separate regional fracture trends from local trends. In this paper, we compare existing
89 interpretations of basin-scale (>1 km scale) faults with the outcrop-scale fracture data. Using
90 field observations, we present possible hypotheses of how discrete discontinuities or
91 pervasive mechanical anisotropies in the basement, such as bedding, fold axial planar
92 foliations, faults, and rheological boundaries, affect deformation in the cover rocks during the
93 syn-rift and post-rift (inversion) stages of basin development. Our findings show that the
94 orientations of fractures that have been influenced by pre-existing basement structures vary
95 between scales of observation.

96 **2. GEOLOGICAL SETTING**

97 **2.1. Structural elements and evolution of the Gippsland Basin**

98 The Gippsland Basin is part of the Australian Southern Margin rift system, which formed
99 during Jurassic–Cretaceous, broadly N-S directed rifting between Australia and Antarctica
100 (Miller et al., 2002 and references therein). Different regional paleo-extension directions,
101 ranging from NW-SE (Willcox and Stagg, 1990; Willcox et al., 1992; O’Brien et al., 1994;
102 Power et al., 2001) to N-S and NNE-SSW (Etheridge et al., 1985; Hill et al., 1994, 1995;
103 Finlayson et al., 1996; Chantraprasert et al., 2001; Krassay et al., 2004), have been inferred
104 for rifting of the Gippsland Basin based on the orientations of rift-related faults. The
105 Gippsland Basin is characterised by three main sets of rift and subsequent reactivation-related
106 faults (Fig. 1). NE-SW and ENE-WSW striking, reverse-reactivated normal faults are
107 dominant in the western onshore part of the basin. Fault and anticline traces in the eastern

108 onshore part of the basin trend roughly E-W, and normal fault traces in the eastern offshore
109 part trend mostly WNW-ESE to NW-SE (Constantine, 2001; Power et al., 2001). Power et al.
110 (2003) proposed that two stages of extension occurred: the first-stage NW-SE extension was
111 followed by a second-stage NE-SW or NNE-SSW extension (Fig. 2). At a broader scale,
112 palinspastic rift reconstructions support NNW-SSE to N-S lithospheric extension between the
113 onset of Australian Southern Margin rifting at ~160 Ma and break-up at ~83.5 (Williams et
114 al., 2011), with an increase in rift obliquity occurring at ca. 100 Ma (Matthews et al., 2012;
115 Müller et al., 2016).

116 It is possible that variable rift fault orientations in the Gippsland Basin are controlled by
117 lateral or temporal changes in regional extension directions. However, the changes in
118 orientation may instead reflect the local influence of pre-existing structures in the underlying
119 basement. Samsu et al. (2019) suggested that NE-SW to ENE-WSW trending syn-rift faults
120 in the Early Cretaceous cover rocks of the western onshore Gippsland Basin (Fig. 3) have
121 orientations that are oblique to those expected from N-S or NNE-SSW directed regional
122 extension proposed in existing literature due to the influence of an underlying anisotropic,
123 heterogeneous basement. Similarly, the lateral change in Early Cretaceous normal fault
124 orientations in the neighbouring Otway Basin coincides with the boundary between two
125 rheologically different basement domains, which may have resulted in the local rotation of
126 extension directions (Miller et al., 2002).

127 Rifting in the Gippsland Basin began in the Early Cretaceous (Fig. 2), first forming syn-
128 depositional normal faults in the onshore Gippsland Basin that trend NE-SW to E-W
129 (Willcox et al., 1992) (Fig. 1). Rifting was interrupted by a period of uplift and inversion at
130 the end of the Early Cretaceous (Dumitru et al., 1991; Duddy and Green, 1992; Foster and
131 Gleadow, 1992; Willcox et al., 1992; Samsu et al., 2019). This event was associated with
132 NNW-SSE oriented shortening, which reactivated NE-SW and ENE-WSW striking rift-

133 related normal faults in a reverse sense and also formed NE-SW and ENE-WSW trending
134 anticlines in the onshore part of the basin (Norvick and Smith, 2001). Rifting then resumed
135 and continued into the Late Cretaceous, during which time E-W to NW-SE trending rift-
136 related faults (e.g., the Rosedale and Foster fault systems; Fig. 1) formed in the eastern
137 onshore and offshore Gippsland Basin (Power et al., 2003). The post-rift Cenozoic history
138 records additional tectonic episodes associated with compression and a NNW-SSE oriented
139 maximum horizontal stress. The stress state has not changed significantly since this time, as
140 the present-day in-situ stress is characterised by a NW-SE oriented ($130 \pm 20^\circ$) maximum
141 horizontal stress determined from borehole breakouts (Hillis and Reynolds, 2000).

142 <Insert Figure 2 here>

143 **2.2 Structural descriptions of cover and basement rocks**

144 This paper discusses the interaction between the two basement units underneath the
145 Gippsland Basin – the folded and faulted Paleozoic basement and a deeper Neoproterozoic–
146 Cambrian basement – and the syn-rift Lower Cretaceous Strzelecki Group cover rocks that
147 unconformably overlie the basement. The following sections provide a brief overview of the
148 geology and structural trends within these three units.

149 <Insert Figure 3 here>

150 **2.2.1 *Cretaceous cover rocks***

151 Rocks of the Lower Cretaceous Strzelecki Group are exposed in cliffs and wave-cut
152 platforms along the coastline near San Remo and in the Cape Paterson area (Fig. 3). These
153 outcrops comprise alternating layers of mud-dominated and sand-dominated siliciclastic
154 rocks with conglomeritic or organic matter-rich interbeds, which were deposited in a fluvial
155 setting (Constantine, 2001). Dip angles of bedding are low, varying between 6° and 26°
156 (Aghaei et al., 2017). High-angle changes in the strike of bedding occur across faults, some

157 of which extend seawards beyond the wavecut platforms, where they can be interpreted from
158 bathymetry data (Samsu et al., 2019). NW-SE to NNW-SSE trending dolerite dykes of
159 Cretaceous age crosscut the Strzelecki Group, exploiting older NW-SE and NNW-SSE
160 striking faults and sub-vertical joints (Duddy and Green, 1992; Constantine, 2001; Samsu et
161 al., 2019).

162 ENE-WSW trending faults in Cretaceous cover rocks (Fig. 3) are Early Cretaceous rift-
163 related faults that were reactivated during a subsequent Early Cretaceous shortening event
164 (Samsu et al., 2019). This phase of NNW-SSE directed maximum horizontal compression
165 was also responsible for NNW-SSE jointing at Harmers Haven (Cape Paterson area; Fig. 3).
166 N-S to NNE-SSW trending faults crop out along the coast between Harmers Haven and
167 Inverloch (in the Cape Paterson area) and appear as up to ~20 m wide fracture zones in near-
168 shore bathymetry data (Fig. 4). Similarities in their orientation and kinematics with pre-rift
169 basement faults, such as the Waratah Fault and Selwyn Fault (Gray et al., 1999; Gardner et
170 al., 2009; Samsu et al., 2019), suggest that they could have formed in association with
171 reactivation of NNE-SSW trending basement fractures.

172 <Insert Figure 4 here>

173 **2.2.2 The Paleozoic basement**

174 The eastern onshore and offshore parts of the Gippsland Basin, which lie east of our study
175 area, overlie the Tabberabbera, Kuark, and Mallacoota Zones of the Lachlan Orogen
176 (VandenBerg et al., 2000) (Fig. 1). The western onshore part of the Gippsland Basin, which is
177 the focus of this study, is underlain by Paleozoic rocks of the Melbourne Zone. The
178 Melbourne Zone exhibits a range of Paleozoic structural trends, from NNW-SSE to NNE-
179 SSW, as a result of folding and thrusting associated with E-W shortening during the Middle
180 Devonian Tabberabberan Orogeny (VandenBerg et al., 2000). North of the Gippsland Basin,

181 major faults and fold axial traces trend predominantly NNW-SSE, with the exceptions in the
182 northernmost part of the Melbourne Zone, where E-W trending faults and fold axial traces
183 may indicate an episode of N-S shortening that postdates the E-W shortening (VandenBerg et
184 al., 2000).

185 Underneath the western onshore Gippsland Basin, a NNE-SSW structural trend can be
186 observed in Ordovician rocks that crop out on the Mornington Peninsula and Devonian rocks
187 that are exposed at Cape Liptrap (Keetley et al., 2001; Cayley et al., 2002; Vollgger and
188 Cruden, 2016) (Fig. 3). Exposed Paleozoic faults trend NNE-SSW (Gray et al., 1999; Cayley
189 et al., 2002), such as the Waratah Fault, Bell Point Fault, and Selwyn Fault (Fig. 3). The
190 Waratah Fault, which is exposed along the southeastern side of Cape Liptrap, has been
191 reactivated multiple times, up until the Holocene (Gardner et al., 2009). The seismically
192 active Selwyn Fault follows the western margin of the Mornington Peninsula (Fig. 3)
193 (Willcox et al., 1992; Cayley et al., 2002). Because of the high contrast in the magnetic
194 characteristics of the rocks on either side of the Selwyn Fault and the length of the fault, it is
195 interpreted that this structure links down into older faults in the Neoproterozoic–Cambrian
196 basement that were active during the Cambrian Tyennan Orogeny (Cayley et al., 2002). The
197 spacing between these deep crustal faults is relatively wide – for example, the Waratah Fault
198 and Selwyn Fault are ~100 km apart.

199 ***2.2.3 The Neoproterozoic–Cambrian basement***

200 The Paleozoic Melbourne Zone unconformably overlies the Neoproterozoic–Cambrian
201 Selwyn Block (Cayley et al., 2002; McLean et al., 2010) (Fig. 1). Folds in the Melbourne
202 Zone, which formed during the Tabberabberan Orogeny, have longer wavelengths and lower
203 amplitudes than those in the adjacent zones, to the west and east, respectively. Therefore, it
204 has been inferred that the underlying Selwyn Block is more rigid than the surrounding lower

205 crust and that it shielded the Melbourne Zone from extensive deformation (VandenBerg et
206 al., 2000).

207 The Selwyn Block comprises metasedimentary and metavolcanic rocks of Neoproterozoic–
208 Cambrian age that were accreted onto the east Gondwanaland margin during the Late
209 Cambrian Delamerian Orogeny (Cayley, 2011). The Cambrian minimum age for regional
210 deformation is defined by an unconformity above Selwyn Block rocks, which crop out at
211 several locations, including at Cape Liptrap (Cayley et al., 2002; VandenBerg et al., 2006).
212 The Selwyn Block comprises several lithological and structural units, as indicated by N-S to
213 NE-SW trending magnetic anomalies (Moore et al., 2016). In south-central Victoria a steeply
214 SW-dipping, NW-trending fault displaces Devonian rocks against Cambrian rocks, which has
215 been interpreted as a Cambrian fault that underwent reactivation during the Tabberabberan
216 Orogeny (ca. 380 Ma; Gray and Willman, 1991). The eastern boundary of the Selwyn Block
217 and internal fabrics within the study area, inferred from potential field data and fault
218 orientations in the overlying units (Cayley et al., 2002), trends NE-SW (Fig. 1).

219 **3. METHODS**

220 A multi-scale structural mapping approach was employed to identify correlations between
221 structures in basement and cover rocks. In this study, “fractures” include shear fractures and
222 joints, all of which form when rocks fail in a brittle manner. The term “fault” is used to
223 describe a zone comprising linked segments of shear fractures when the individual shear
224 fractures cannot be recognised at the scale of observation. “Fracture zone” is used for areas of
225 intensely fractured rock, which in wavecut platforms have typically been eroded. The term
226 “joint” is used to describe a fracture that exhibits no offset along its length at the scale of
227 observation. Fractures are considered systematic when they are parallel or sub-parallel or are
228 regularly distributed, hence a fracture set consists of parallel to sub-parallel systematic

229 fractures. Irregularly oriented fractures that demonstrate no obvious spatial relationship to
230 one another are considered to be non-systematic.

231 Outcrop-scale mapping of basement structures was conducted on Melbourne Zone outcrops
232 at Shark Stack (Cape Liptrap, see Fig. 3 for location). Although Cambrian metavolcanic
233 rocks of the Selwyn Block are exposed nearby (Cayley et al., 2002), the highly deformed
234 nature of the outcrop made it unsuitable for collecting structural measurements. Structures at
235 the Shark Stack locality were interpreted from field observations, with the help of
236 orthophotos generated from aerial photographs collected from an unmanned aerial vehicle
237 (UAV) (Vollgger and Cruden, 2019). Previous mapping of basin-scale (>1 km-scale) faults
238 using gravity and magnetic data (Samsu et al., 2019), help to constrain general structural
239 trends and distinguish between pre-rift and syn-rift structures in the basement. Fractures in
240 cover rocks in the Cape Paterson area (see Fig. 3 for location) were traced from UAV
241 orthophotos, which facilitated rapid collection of data on thousands of fractures over a wide
242 area at high spatial resolution. Here we introduce the workflow used for collecting fracture
243 data and for evaluating trends in the orientation of fracture traces.

244 **3.1 Semi-automated fracture tracing**

245 UAV-derived orthophotos of outcrops enabled the collection of fracture data at five outcrop
246 localities (Fig. 4) over a total area of $\sim 0.934 \text{ km}^2$. These orthophotos are suitable for
247 evaluation of fracture variability and clustering across a wide area using the areal sampling
248 method, where fracture traces are mapped in two dimensions (2D) using aerial photographs
249 (Wu and Pollard, 1995; Watkins et al., 2015). As the individual mapped areas were relatively
250 large (up to 0.330 km^2), the likelihood for sampling bias at each map locality – which can be
251 problematic when fracture patterns change with position (Rohrbaugh et al., 2002) – could be

252 reduced. For a summary of the UAV photogrammetry workflow and the parameters chosen
253 for the UAV surveys, see Table 1 in the supporting information (cf. Dering et al., 2019).

254 Fractures at the five outcrop localities – Harmers Haven North, Harmers Haven South, Eagles
255 Nest, The Caves-Flat Rocks, and Inverloch (Fig. 4) – were interpreted using a semi-
256 automated fracture tracing method (Fig. 5). The method, implemented as a QGIS plugin,
257 GeoTrace (Thiele et al., 2017), uses a least-cost path algorithm on a cost function that
258 highlights geological features. We traced fractures that were visible at one chosen scale of
259 1:500 (Fig. 6). We found that tracing fractures at this scale provided a good balance between
260 maximizing the use of the high-resolution orthophotos (down to 1.94 cm/pixel) and limiting
261 the amount of time required to trace all of the observable fractures (up to eight hours for one
262 locality). Our method ensured that when we analysed the orientation of the fracture
263 populations from different localities, we were comparing fractures that were observable at the
264 same scale.

265 <Insert Figure 5 here>

266 <Insert Figure 6 here>

267 **3.2 Fracture orientation analysis using length-coloured rose diagrams**

268 Circular histograms, or rose diagrams, are common statistical plots for analysing the
269 orientation distribution of fractures within a study area (e.g., Marchegiani et al., 2006; Munro
270 and Blenkinsop, 2012; Lavenu et al., 2013; Healy et al., 2017). Unweighted rose diagrams are
271 calculated without discrimination between fractures of different lengths. Weighted rose
272 diagrams are typically calculated by weighting the influence of a fracture's orientation by the
273 fracture length. An alternative to binned rose diagrams are Gaussian smoothed rose diagrams
274 (e.g., Robin and Jowett, 1986), which are useful for accentuating trends in orientation data.
275 While these existing variations of rose diagram types help to identify fracture orientation

276 trends, none of them show the length of the fractures that make up each trend in a rose
277 diagram.

278 In this study, we are interested in the contribution of fractures of different lengths to fracture
279 orientation trends within each outcrop area. Our approach is concerned with whether
280 fractures of different lengths develop different orientations preferentially, therefore testing for
281 scale-dependence. Fracture traces that are relatively long are often straight, continuous joints
282 that have not been offset by subsequent shear fractures. Alternatively, they can represent
283 larger faults, where individual shear fracture segments cannot be recognised at the scale of
284 observation, either due to the close spacing between segment tips or weathering along the
285 fracture. Shorter fracture traces mostly represent joints, shear fractures, or non-systematic
286 fractures.

287 Here we present a new technique for characterizing the trends in a fracture population, where
288 the distribution of fracture length is plotted on an unweighted rose diagram to produce
289 “length-coloured rose diagrams”. These rose diagrams allow for a more comprehensive
290 analysis of the fracture network, showing whether each peak orientation is associated with
291 relatively “short” or “long” fracture traces. The petals of the rose diagram are subdivided into
292 coloured segments that represent the percentage contribution of fractures within each length
293 bin. This method has been implemented in the GeoTrace plugin for QGIS (Thiele et al., 2017;
294 <https://github.com/lachlangrose/GeoTrace>). Fracture orientations were compared between the
295 five different outcrop localities (Fig. 4 and 5). For each locality, all of the fractures that were
296 traced at a scale (or ‘zoom’) of 1:500 were treated as one population, resulting in one rose
297 diagram per locality.

298 **3.3 Fracture orientation analysis using gridded rose diagrams**

299 A second analysis was performed to assess the heterogeneity of fracture patterns within
300 individual outcrop localities, as there is usually significant variation in fracture density or
301 orientations even within a small area. For the Harmers Haven North locality (see Fig. 4 for
302 location), fractures were traced manually at a scale of 1:500. Grid tiles with 100 m by 100 m
303 dimensions were overlain onto the fracture trace map, and a length-weighted binned rose
304 diagram (with 10°-wide bins) was generated for the fracture trace segments in each grid tile,
305 resulting in one rose diagram per grid tile (Fig. 7). Grid tiles that contained less than 30
306 fracture trace segments were excluded from the analysis. This technique is implemented in
307 the Line Direction Histogram plugin (Tveite, 2015) for QGIS. This method allowed us to test
308 the consistency of fracture orientations throughout an outcrop. It also assisted in determining
309 whether clustering or anomalous fracture patterns in a given locality are associated with
310 changes in lithology, structural style, or other factors.

311 <Insert Figure 7 here>

312 **4. RESULTS**

313 **4.1 Structural characteristics of basement rocks (Cape Liptrap)**

314 The Shark Stack outcrop is located near the southwestern tip of Cape Liptrap (Fig. 8). Here,
315 tightly folded turbidites of the Devonian Liptrap Formation are exposed on wavecut
316 platforms and steep, SSW-facing cliffs (Fig. 9 and 10). The rocks comprise steeply dipping,
317 alternating beds of sandstone and mudstone, and they exhibit a first-order NNE-SSW
318 structural trend in map view (Fig. 8c). The sequence of ductile and brittle deformation
319 inferred for the Shark Stack locality is summarised in Table 1, interpreted using observations
320 acquired from both field and UAV-based mapping of structures.

321 <Insert Figure 8 here>

322

<Insert Table 1 here>

323 The strike of bedding in the fold limbs is predominantly NNE-SSW, with beds dipping
324 steeply to sub-vertically towards the ESE and WNW (Fig. 9d). The fold axis calculated from
325 bedding measurements (from across the entire outcrop) trends 198° and plunges 20° , which
326 represents the fold axis of first-generation F1 folds at this locality. This fold axis is consistent
327 with the F1 fold axis reported for the southern part of Fold Stack (201/11; Vollgger and
328 Cruden, 2016), which is located approximately 400 m northeast of Shark Stack (Fig. 8b). A
329 steeply ESE-dipping to sub-vertical, axial planar cleavage is consistent with the bedding
330 measurements and fold axis, suggesting that local shortening was WNW-ESE. We interpret
331 the F1 folds in the area to be related to ~E-W shortening associated with the Devonian
332 Tabberabberan Orogeny (385 – 380 Ma; VandenBerg et al., 2000). Reverse faults with a low
333 strike angle to bedding offset sandstone beds, while associated strain is accommodated by
334 ductile deformation of the mudstone layers.

335

<Insert Figure 9 here>

336 The Shark Stack outcrop contains N-S trending zones of intensely folded beds (Fig. 10). In
337 map view, these structures appear to be either reverse kink bands or disharmonic folds (Fig.
338 10a), though in cross section (along subvertical cliffs) they appear exclusively as disharmonic
339 folds (Fig.10b). Kink band formation in some zones has progressed to chevron folding (Fig.
340 10a). Similar “kink folds” have been observed in shale-rich outcrops at the southernmost tip
341 of Cape Liptrap, ~800 m southeast of Shark Stack. Kink fold hinges plunge mostly to the
342 south (Fig. 9e), consistent with N-S trending axial traces mapped on the 2D dataset (Fig.
343 10a). As the kink folds’ axial traces are oblique to the NNE-SSW trending F1 fold axial
344 traces, we suggest that these F2 kink folds formed during a separate D2 folding event.

345 F2 kink folds may have formed due to NNE-SSW oriented shortening, which was directed
346 sub-parallel to the strike of bedding. This interpretation is based on analogue experiments,
347 field examples, and mechanical experiments of kink bands in anisotropic media, which
348 suggest that reverse kink bands result from local shortening parallel to the anisotropy (e.g.,
349 Cobbold et al., 1971; Stubbley, 1989; Kapp et al., 2016). The dextral sense of shear required to
350 create the observed kink fold geometry, as well as the orientation of the folds, is also
351 consistent with NNE-SSW oriented shortening. Field evidence for N-S to NNE-SSW
352 shortening – including E-W trending folds, north-dipping reverse faults, and steeply dipping,
353 E-W striking axial planar cleavage – at a later stage of the Tabberabberan Orogeny
354 (following E-S shortening) has also been found in the northern part of the Melbourne Zone
355 (Gray and Mortimer, 1996; Wilson et al., 2017).

356 <Insert Figure 10 here>

357 ENE-WSW trending dextral shear fractures and a larger fracture zone of the same orientation
358 (Fig. 8c) is attributed to a D3 brittle deformation event. Like the ENE-WSW trending fracture
359 set at Fold Stack (Vollgger and Cruden, 2016), this set is parallel to Early Cretaceous rift-
360 related normal faults within the Lower Cretaceous Strzelecki Group (Samsu et al., 2019).
361 They are the only structures at Shark Stack that can be associated with Early Cretaceous
362 Gippsland Basin rifting.

363 A D4 deformation event is associated with a NW-SE trending kink band zone that extends
364 across the middle and along the length of the entire Shark Stack outcrop, overprinting F2 kink
365 bands (Fig. 8c and 10). In this <3.3 m wide zone, the local sense of shear is dextral, and the
366 kinks offset the sandstone and mudstone layers laterally by <1 m. Smaller, less developed
367 kink bands of the same orientation are also present. A NNW-SSE trending set of sinistral
368 fractures occurs in the northwest section of the outcrop (Fig. 8c). The acute bisector between

369 the F4 kink bands and the NNW-SSE fractures is $\sim 30^\circ$. Based on the orientation and
370 kinematics of the F4 kink bands and the NNW-SSE trending fracture set, we interpret them as
371 conjugate structures that formed during a phase of NNW-SSE directed D4 shortening. The
372 relative timing of D3 fractures and D4 kinks is ambiguous – the large ENE-WSW trending
373 fracture zone potentially offsets NW-SE trending kink bands in the orthophoto (Fig. 8c), but
374 the amount of weathering in this part of the outcrop makes it difficult to confirm this. As the
375 two sets are orthogonal to each other and both exhibit a dextral sense of movement, they
376 cannot have formed coevally.

377 Most of the NW-SE trending structures at Shark Stack that were mapped using the UAV
378 orthophoto are short F4 kink bands (<10 m in length) (Fig. 11). Longer fractures (>10 m) are
379 associated with NNW-SSE and ENE-WSW trending fracture sets. These fractures are
380 relatively young D3 and D4 structures compared to pre-rift D1 and D2 structures and show
381 high lateral continuity because they have not been overprinted by younger structures.

382 <Insert Figure 11 here>

383 **4.2 The orientation of fractures in cover rocks (Cape Paterson area)**

384 Fracture orientation trends in the Strzelecki Group cover rocks in the Cape Paterson area (see
385 Fig. 3 for location) are presented as rose diagrams (Fig. 4 and 5) and summarised in Table 2.
386 Here we describe fracture orientations at five outcrop localities – Harmers Haven North,
387 Harmers Haven South, Eagles Nest, the Caves – Flat Rocks, and Inverloch – and use peaks in
388 the data to classify fracture traces into fracture sets. We also use overprinting relationships
389 between fracture traces in the UAV orthophotos and field observations to identify the type of
390 fractures that make up each fracture set.

391 <Insert Table 2 here>

392 The predominant trend at Harmers Haven North is NNW-SSE (335–350°) (Fig. 5a). This
393 fracture set comprises linear, systematic joints that are parallel to – and are potentially
394 exploited by – NNW-SSE trending mafic dykes. We observe two other peaks in the data for
395 this locality: WNW-ESE (280–295°) and E-W (080–100°), which correspond to shear
396 fractures. These two sets are more prevalent in the central part of the outcrop, while the
397 NNW-SSE trending set is more dominant in the western and eastern parts of the outcrop. The
398 longer (>30 m) fracture traces at this locality are faults across which the strike of bedding
399 changes significantly. A more detailed discussion of the spatial variability of fracture trends
400 at Harmers Haven North (Fig. 7) is presented below.

401 At Harmers Haven South, one wide peak in the rose diagram is present, trending NNW-SSE
402 (325–345°) (Fig. 5d). The NNW-SSE fracture set consists mostly of joints, some of which are
403 exploited by NNW-SSE trending mafic dykes at the northern end of the outcrop. Faults trend
404 NW-SE and some of them are also exploited by NW-SE trending mafic dykes.

405 The Eagles Nest locality was split into a southern and northern area (Fig. 5b). The rose
406 diagram of fracture traces in both areas combined show a dominant NNW-SSE (325–345°)
407 peak. The second most dominant trend is represented by a wide peak, trending ENE-WSW
408 (065–080°) and E-W (080–095°). In the southern area, NNW-SSE and ENE-WSW trending
409 systematic fracture sets, which are mutually crosscutting, are present near the Eagles Nest
410 pinnacle. The ENE-WSW trending normal fault slightly north of the pinnacle is associated
411 with Early Cretaceous rifting. A NE-SW trending fracture set is confined to a small area west
412 of the pinnacle. In the northern area, a large N-S trending fracture zone bounds the Eagles
413 Nest locality to the east. The N-S trending fault truncates an ENE-WSW trending fault and
414 the NNW-SSE fracture set to the west. The significant rotation of sedimentary beds across
415 this fault and the syn-sedimentary nature of ENE-WSW trending normal faults in the area
416 (Samsu et al., 2019) suggests that the N-S fault postdates ENE-WSW normal faulting.

417 At the Caves – Flat Rocks, the main peak in the rose diagram corresponds to NNW-SSE
418 (320–345°) trending shear fractures (Fig. 5e). The second-most dominant peak is associated
419 with ENE-WSW (065–085°) trending fractures, some of which are normal faults associated
420 with Early Cretaceous rifting. A third, less dominant NNE-SSW (010-020°) trend is made up
421 of shear fractures. ENE-WSW trending faults are offset by NNW-SSE and NNE-SSW
422 trending shear fractures, which may explain why this fracture set has the highest percentage
423 of shorter (<10 m) fractures relative to their frequency. The Inverloch locality is populated by
424 fractures that are shorter than 20 m (Fig. 5c). One sharp E-W trending peak (085 – 095°) and
425 another sub-population of WNW-ESE to NNW-SSE (290 – 345°) trending fractures are
426 represented in the rose diagram.

427 A common occurrence among the five described localities is the presence of a NNW-SSE
428 trending fracture set, which mostly consists of sub-vertical joints. This joint set is interpreted
429 to be a pervasive, regional outcrop-scale joint set that reflects Early Cretaceous shortening
430 (Samsu et al., 2019), which postdates Early Cretaceous syn-rift normal ENE-WSW faulting
431 and predates the Aptian intrusion of NW-SE and NNW-SSE trending mafic dykes in the
432 study area. The formation of this joint set could also be coeval with reverse reactivation of
433 the optimally oriented, aforementioned ENE-WSW trending normal faults, which agrees with
434 an interpretation by Power et al. (2003) of similarly orientated compressional structures in the
435 offshore Gippsland Basin.

436 ***4.2.1 Variability of fracture orientations within the Harmers Haven North locality***

437 The Harmers Haven North outcrop was subdivided into three domains based on the main
438 fracture orientations (Table 2; Fig. 7). The western section of the outcrop (Domain A)
439 exhibits a dominant NNW-SSE trending fracture set. Field observations confirm that this set
440 is made up of joints, similar to the NNW-SSE trending fracture set at Harmers Haven South.

441 Domain A also contains a single NNW-SSE trending dyke that is parallel with the main joint
442 set. A less prominent E-W trending fracture set is present in Domain A. The middle section
443 of the outcrop (Domain B) exhibits a dense network of approximately E-W trending, non-
444 systematic shear fractures. Three NNE-SSW trending shear fractures in Domain B
445 (represented by thick red lines in Fig. 7) correspond to km-scale faults interpreted from near-
446 shore bathymetry (Fig. 4). The eastern section of the outcrop (Domain C) exhibits the same
447 NNW-SSE joint set as observed in Domain A, although fractures of other orientations are
448 also present.

449 **4.2.2 *Curved fractures at the Eagles Nest locality***

450 The most dominant fracture set at Eagles Nest is the NNW-SSE trending set of up to 50 m
451 long fractures (Fig. 12). NNW-SSE trending fractures in the northern area curve eastwards
452 into the N-S trending fracture zone. There is no evidence of shear along these NNW-SSE
453 trending fractures, so they can be interpreted as joints, like the NNW-SSE trending joints at
454 Harmers Haven North and Harmers Haven South (Table 2). The curved NNW-SSE joints at
455 Eagles Nest are comparable with joints that “veer” from linearity (Cruikshank and Aydin,
456 1995) as they propagate into a changing stress field, which may result from stress
457 perturbations near pre-existing structures. Photoelastic experiments on analogue materials
458 (e.g., de Joussineau et al., 2003) demonstrate the deviation of stress trajectories near pre-
459 existing defects (analogous to faults in rocks) under a biaxial compressive load. Welch et al.
460 (2014) discuss the development of local stress anomalies near tips, bends and splays in larger
461 faults. At Eagles Nest, veering of the NNW-SSE joints would have resulted from the
462 divergence of local maximum principal stress trajectories from the regional shortening, which
463 was due to local stress perturbations around the large N-S trending fracture zone.

464 <Insert Figure 12 here>**5. DISCUSSION**

465 **5.1 Rift faults oblique to basement structures and the regional extension direction**

466 In the western onshore Gippsland Basin, NNE-SSW striking faults in the Neoproterozoic–
467 Cambrian Selwyn Block basement were reactivated during Devonian deformation of the
468 shallower Melbourne Zone basement, forming the Waratah and Selwyn faults. In contrast to
469 these contractional structures, Cretaceous normal syn-rift faults in the study area trend NE-
470 SW to ENE-WSW, oblique to NNE-SSW striking basement faults and foliation. These syn-
471 rift faults are also oblique to their expected E-W orientation, given the E-W orientation of
472 syn-rift faults in the eastern portion of the Gippsland Basin and the N-S to NNE-SSW
473 regional extension inferred in the literature (Etheridge et al., 1985; Hill et al., 1994, 1995;
474 Finlayson et al., 1996; Chantraprasert et al., 2001; Krassay et al., 2004).

475 Reactivation of basement structures ought to have resulted in NNE-SSW trending normal
476 faults that are parallel to pre-existing planar basement weaknesses (cf. Holdsworth et al.,
477 1997; Kirkpatrick et al., 2013; Phillips et al., 2016). Hodge et al. (2018) have shown, using
478 field observations from the Malawi Rift System in East Africa, that faults can form oblique to
479 the reactivated basement foliation. However, these foliation-oblique faults exhibit variable
480 strike and form links between en échelon, foliation-parallel fault scarps. In our western
481 onshore Gippsland Basin case study, the syn-rift faults are parallel to each other, forming a
482 systematic NE-SW to ENE-WSW trending set. We therefore argue that a more widespread
483 rotation of the local extension direction (caused by the underlying pervasive basement
484 anisotropy) contributed to the obliquity of these faults as opposed to localised strain or stress
485 rotations along a single structure. These observations suggest that a mechanism other than
486 reactivation may be responsible for inheritance-influenced, syn-rift normal faulting (Fig.
487 13b).

488 <Insert Figure 13 here>

489 Existing research on inheritance in rift basins largely focuses on reactivation (e.g., Whipp et
490 al., 2014; Phillips et al., 2016; Fazlikhani et al., 2017; Collanega et al., 2019; Heilman et al.,
491 2019). We suggest that a second, poorly understood mechanism of structural inheritance
492 involves a rotation or perturbation of the local extension direction above an anisotropic
493 basement unit with a structural trend that is oblique to the rifting direction. Our observations
494 are comparable with the results of field studies from north-western Scotland (Wilson et al.,
495 2010) and the East African rift system (Morley, 2010), where fracture orientations vary
496 between areas that have different basement domains. Lateral changes in fracture orientation
497 act as evidence for localised rotations of strain (Philippon et al., 2015; Williams et al., 2019),
498 which may reflect local perturbations or re-orientation of the far-field stress.

499 **5.2 The influence of multiple levels of basement on cover faults**

500 Two depth levels of basement beneath the western onshore Gippsland Basin study area likely
501 had an impact on basin formation (Fig. 1). Both levels of basement were subjected to
502 multiple shortening events prior to Early Cretaceous rifting and opening of the Gippsland
503 Basin, resulting in a first-order NNE-SSW structural trend (Gray et al., 1999; Cayley et al.,
504 2002; McLean et al., 2010; Moore et al., 2016) that is oblique to subsequent Cretaceous rift-
505 related structures. NNE-SSW trending faults in the Melbourne Zone formed as a result of
506 roughly E-W shortening during the Devonian Tabberabberan Orogeny. Some of these faults,
507 such as the Waratah and Selwyn faults, extend into the underlying Selwyn Block basement,
508 so it has been suggested that reactivation of Selwyn Block faults exerted some control on
509 Devonian deformation in the Melbourne Zone basement (Cayley, 2011) (A in Fig. 13a).
510 Based on field observations of NNE-SSW striking D1 structures at Shark Stack and Fold
511 Stack (Vollgger and Cruden, 2016) (Cape Liptrap; Fig. 9) and similarly trending faults and
512 formlines in Paleozoic rocks on the Mornington Peninsula (~100 km northwest of Cape

513 Liptrap; Fig. 3) (Cayley et al., 2002; McLean et al., 2010), we infer that the Melbourne Zone
514 basement beneath our mapped Cretaceous cover outcrops (Cape Paterson area; Fig. 3)
515 exhibits a penetrative NNE-SSW trending anisotropy. The mechanical anisotropy created by
516 alternating mudstone and sandstone units has the potential to locally perturb the regional
517 stress field. Alternatively, relatively weak mudstone layers between competent sandstone
518 layers may be prone to re-shearing when the crust is subject to later extension or
519 compression. This anisotropy should have exerted a greater influence on regional faulting
520 patterns in the cover compared to less pervasive, more localised fractures (B in Fig. 13a).

521 The postulated eastern boundary of the Selwyn Block (and the overlying Melbourne Zone)
522 was partly defined by a change from NE-SW and ENE-WSW trending faults in the western
523 onshore part of the Gippsland Basin to E-W trending faults in the eastern onshore and
524 offshore parts (Cayley et al., 2002) (Fig. 1). The lower crustal Selwyn Block is inferred to be
525 more rigid than the surrounding lower crust (Cayley et al., 2002; Teasdale et al., 2004), so
526 that the Selwyn Block boundary separates an anomalously strong lower crustal block from
527 the “normal” lower crust. The strength contrast between the Selwyn Block and the adjacent,
528 weaker, lower crust could be an additional source of local strain re-orientation that
529 contributed to the extension-oblique orientation of the rift faults in the cover (C in Fig. 13a).

530 **5.3 Structural inheritance is not scale-invariant**

531 Multi-scale mapping of fracture traces allowed comparison between: 1) the orientations of
532 outcrop-scale basement and cover structures, and 2) the orientations of basin-scale (>1 km-
533 scale) fractures and outcrop-scale (meters to tens of meters-scale) fractures. By comparing
534 D3 and D4 basement structures with cover fractures, we observed that a single tectonic event
535 can be reflected by different fracture trends in basement and cover rocks, likely due to
536 differences in the mechanical anisotropy. Outcrop-scale cover fractures in our study area

537 have trends that are different to outcrop-scale basement fractures, with the exception of the
538 ENE-WSW trending fracture set (Fig. 3 and 4). Syn-rift normal faults exhibit the same ENE-
539 WSW trend at both basin scale and outcrop scale (Fig. 14a).

540 <Insert Figure 14 here>

541 The trends of outcrop-scale fractures that formed during NNW-SSE shortening are different
542 from the trends of basin-scale (>1 km-long) fractures (Fig. 14b); joints formed at the small
543 scale, but reverse reactivation of normal faults occurred at the large scale. The persistent
544 NNW-SSE peak in the outcrop-scale fracture data highlights the abundance and
545 pervasiveness of a NNW-SSE trending subvertical joint set in the Strzelecki Group cover
546 rocks across the entire study area. Samsu et al. (2019) have discussed the formation of this
547 joint set under NNW-SSE directed maximum horizontal stress, coeval with a conjugate set of
548 NNW-SSE and N-S to NNE-SSW trending strike-slip faults, and reactivation of optimally
549 oriented NNE-SSW striking basement faults in a strike-slip sense, which explains the NNE-
550 SSW fracture trend in the rose diagram for >1 km-scale faults (Fig. 14b). This event may
551 have coincided with Early Cretaceous (Aptian) basin uplift and the reverse reactivation of
552 ENE-WSW rift faults during basin inversion (Holdgate et al., 2003; Power et al., 2003).

553 Aptian contractional structures are associated with NNW-SSE directed maximum horizontal
554 stress and reflect different stress states. The first group of structures, comprising NNW-SSE
555 trending joints, conjugate strike-slip faults, and strike-slip reactivated NNE-SSW striking
556 basement faults, would have required a horizontal least principal stress (σ_3). The second
557 group, comprising ENE-WSW striking normal faults that have been reactivated in a reverse
558 sense, would have required a vertical σ_3 . By drawing comparisons with Van Noten et al.
559 (2012) on the evolution of the 3D stress field during tectonic inversion, we infer that the two
560 groups of structures were active at different stages of basin inversion. The first group could

561 have been active during an earlier stage of basin inversion, and the second group is associated
562 with a later stage of inversion after σ_3 switched from horizontal to vertical (and the opposite
563 occurred for the intermediate stress, σ_2). It is therefore possible that temporal changes in the
564 stress field contribute to the scale-dependent nature of structural inheritance, though this
565 relationship requires further exploration.

566 At outcrop scale, NNW-SSE trending joints behave differently near large faults that either
567 pre-date or are coeval with joint formation. At Eagles Nest, the joints veer into
568 perpendicularity with a large N-S trending fracture zone that may have locally perturbed far-
569 field stress trajectories (Fig. 12). This joint set is absent adjacent to NNE-SSW trending faults
570 at Harmers Haven North. Our results imply that outcrop-scale fractures (such as joints) may
571 be faithful recorders of the far-field stress when not affected by adjacent larger faults, which
572 serve to alter the local stress field.

573 **6. CONCLUSIONS**

574 Pre-existing basement structures exert significant control on the orientation and distribution
575 of fractures in the sedimentary cover rocks of a rift basin. However, this basement influence
576 manifests itself differently at different scales. Inheritance does not always result in cover
577 fractures that are parallel to basement structures, which is expected with basement
578 reactivation. In the western onshore Gippsland Basin, both basin-scale and outcrop-scale syn-
579 rift faults are oblique to the basement trends as well as their expected orientation based on the
580 inferred regional paleo-extension direction, suggesting that stresses above the basement
581 structures were perturbed such the extension direction was locally rotated, and faults in the
582 cover rocks became misaligned to both their expected orientation and the basement
583 anisotropy. This finding should motivate us to explore and model the mechanisms of

584 structural inheritance, other than reactivation, through additional field-based studies as well
585 as analogue and numerical experiments.

586 When attempting to understand the influence of structural inheritance on deformation in a rift
587 basin, it is important to consider not just the basement that directly underlies the sedimentary
588 cover, but older, deeper basement units as well. As multiple levels of basement are often
589 present, it is challenging to distinguish the relative contributions of pre-existing structures
590 from each basement unit. In our study area, widely spaced faults in the deeper
591 Neoproterozoic–Cambrian Selwyn Block basement were reactivated during Devonian
592 deformation of the shallower Melbourne Zone basement. Because these faults appear to have
593 been reactivated again during subsequent, post-rift deformation of the cover rocks, it is
594 evident the Selwyn Block basement faults influence structural geometry over multiple
595 tectonic events, albeit at a large scale. The pervasive anisotropy of the Melbourne Zone may
596 have exerted a greater control than the Selwyn Block faults on more closely-spaced fractures
597 (i.e., Cretaceous rift-related normal faults). This example shows the importance of mapping
598 structures in all of the basement units, at multiple scales, to explore the possibility of different
599 wavelengths of basement influence.

600 Our findings demonstrate that in basins influenced by structural inheritance, fracture patterns
601 are not scale-invariant. A proper understanding of the structural architecture can only be
602 achieved by analysing data that span multiple scales. This observation is relevant when we
603 try to understand and predict the distribution and orientation of fractures – at regional, basin,
604 and reservoir-scale – in order to model fluid transport in the crust. This study also highlights
605 the importance of mapping fractures in outcrop analogues of naturally fractured reservoirs.

606 **ACKNOWLEDGEMENTS**

607 We thank Sam Thiele, Megan Withers, and Jonas Köpping for their assistance with data
608 collection. Åke Fagereng and an anonymous reviewer are thanked for their constructive
609 reviews. Fieldwork was partly funded by an AAPG Grants-in-Aid Award awarded to AS. AS
610 and SAV were supported by a Monash University Faculty of Science Dean's International
611 Postgraduate Research Scholarship.

612 **DATA AVAILABILITY**

613 The basemap used for structural mapping at Shark Stack (Cape Liptrap) is available at 10 cm
614 resolution from <https://doi.org/10.26180/5c653193efa25> (Vollgger and Cruden, 2019). The
615 datasets used for fracture mapping at Harmers Haven North, Harmers Haven South, Eagles
616 Nest, the Caves–Flat Rocks, and Inverloch are available from
617 <https://doi.org/10.26180/5cdcad0a73fe0> (Samsu et al., 2019).

618 **REFERENCES**

- 619 Aghaei, H., Hall, M., Wagstaff, B., Tait, A., 2017. Stratigraphic reconstruction of the
620 Strzelecki Group outcrops in west Gippsland: new data on the present-day thickness and
621 amount of erosion. *Australian Journal of Earth Sciences* 64, 251–264.
622 <https://doi.org/10.1080/08120099.2016.1278033>
- 623 Bourne, S.J., Willemsse, E.J.M., 2001. Elastic stress control on the pattern of tensile fracturing
624 around a small fault network at Nash Point, UK. *Journal of Structural Geology* 23,
625 1753–1770. [https://doi.org/https://doi.org/10.1016/S0191-8141\(01\)00027-X](https://doi.org/https://doi.org/10.1016/S0191-8141(01)00027-X)
- 626 Byerlee, J., 1978. Friction of rocks. *Pure and Applied Geophysics* 116, 615–626.
627 <https://doi.org/10.1007/BF00876528>
- 628 Cayley, R.A., 2011. Exotic crustal block accretion to the eastern Gondwanaland margin in the
629 Late Cambrian-Tasmania, the Selwyn Block, and implications for the Cambrian-Silurian

630 evolution of the Ross, Delamerian, and Lachlan orogens. *Gondwana Research* 19, 628–
631 649. <https://doi.org/10.1016/j.gr.2010.11.013>

632 Cayley, R.A., Taylor, D.H., VandenBerg, A.H.M., Moore, D.H., 2002. Proterozoic - Early
633 Palaeozoic rocks and the Tyennan Orogeny in central Victoria: The Selwyn Block and
634 its tectonic implications. *Australian Journal of Earth Sciences* 49, 225–254.
635 <https://doi.org/10.1046/j.1440-0952.2002.00921.x>

636 Chantraprasert, S., McClay, K.R., Elders, C., 2001. 3D Rift Fault Systems of the Western
637 Otway Basin, SE Australia. In: Hill, K.C., Bernecker, T. (Eds.), *Eastern Australasian*
638 *Basins Symposium*. Petroleum Exploration Society of Australia, Melbourne, 435–446.

639 Cobbold, P.R., Cosgrove, J.W., Summers, J.M., 1971. Development of internal structures in
640 deformed anisotropic rocks. *Tectonophysics* 12, 23–53. [https://doi.org/10.1016/0040-](https://doi.org/10.1016/0040-1951(71)90065-5)
641 [1951\(71\)90065-5](https://doi.org/10.1016/0040-1951(71)90065-5)

642 Collanega, L., Jackson, C.A., Bell, R.E., Coleman, A.J., Lenhart, A., Breda, A., 2019.
643 Normal fault growth influenced by basement fabrics: the importance of preferential
644 nucleation from pre-existing structures. *Basin Research* in press.
645 <https://doi.org/10.1111/bre.12327>

646 Constantine, A., 2001. *Sedimentology, Stratigraphy and Palaeoenvironment of the Upper*
647 *Jurassic-Lower Cretaceous Non-Marine Strzelecki Group, Gippsland Basin,*
648 *Southeastern Australia*. Monash University. PhD Thesis.

649 Corti, G., van Wijk, J., Cloetingh, S., Morley, C.K., 2007. Tectonic inheritance and
650 continental rift architecture: Numerical and analogue models of the East African Rift
651 system. *Tectonics* 26, 1–13. <https://doi.org/10.1029/2006TC002086>

652 Cruikshank, K.M., Aydin, A., 1995. Unweaving the joints in Entrada Sandstone, Arches

653 National Park, Utah, U.S.A. *Journal of Structural Geology* 17, 409–421.
654 [https://doi.org/10.1016/0191-8141\(94\)00061-4](https://doi.org/10.1016/0191-8141(94)00061-4)

655 de Joussineau, G., Petit, J.P., Gauthier, B.D.M., 2003. Photoelastic and numerical
656 investigation of stress distributions around fault models under biaxial compressive
657 loading conditions. *Tectonophysics* 363, 19–43. [https://doi.org/10.1016/S0040-](https://doi.org/10.1016/S0040-1951(02)00648-0)
658 [1951\(02\)00648-0](https://doi.org/10.1016/S0040-1951(02)00648-0)

659 Dering, G.M., Micklethwaite, S., Thiele, S.T., Vollgger, S.A., Cruden, A.R., 2019. Review of
660 drones, photogrammetry and emerging sensor technology for the study of dykes: Best
661 practises and future potential. *Journal of Volcanology and Geothermal Research*.
662 <https://doi.org/10.1016/j.jvolgeores.2019.01.018>

663 Duddy, I.R., Green, P.F., 1992. Tectonic development of the Gippsland Basin and environs:
664 identification of key episodes using Apatite Fission Track Analysis (AFTA). *Gippsland*
665 *Basin Symposium* 22-23 June 1992. Melbourne, 111–120.

666 Dumitru, T.A., Hill, K.C., Coyle, D.A., Duddy, I.R., Foster, D.A., Gleadow, A.J.W., Green,
667 P.F., Kohn, B.P., Laslett, G.M., O’Sullivan, P.B., 1991. Fission track thermochronology:
668 Application to continental rifting of south-eastern Australia. *The APEA Journal* 31,
669 131–142.

670 Etheridge, M.A., Branson, J.C., Stuart-Smith, P.G., 1985. Extensional basin-forming
671 structures in Bass Strait and their importance for hydrocarbon exploration. *The APEA*
672 *Journal* 25, 344–361.

673 Fazlikhani, H., Fossen, H., Gawthorpe, R.L., Faleide, J.I., Bell, R.E., 2017. Basement
674 structure and its influence on the structural configuration of the northern North Sea rift.
675 *Tectonics* 36, 1151–1177. <https://doi.org/10.1002/2017TC004514>

676 Finlayson, D.M., Johnstone, D.W., Owen, A.J., Wake-Dyster, K.D., 1996. Deep seismic
677 images and the tectonic framework of early rifting in the Otway Basin, Australian
678 southern margin. *Tectonophysics* 264, 137–152. [https://doi.org/10.1016/S0040-](https://doi.org/10.1016/S0040-1951(96)00123-0)
679 [1951\(96\)00123-0](https://doi.org/10.1016/S0040-1951(96)00123-0)

680 Foster, D.A., Gleadow, A.J.W., 1992. Reactivated tectonic boundaries and implications for
681 the reconstruction of southeastern Australia and northern Victoria Land, Antarctica.
682 *Geology* 20, 267–270. [https://doi.org/10.1130/0091-](https://doi.org/10.1130/0091-7613(1992)020<0267:RTBAIF>2.3.CO;2)
683 [7613\(1992\)020<0267:RTBAIF>2.3.CO;2](https://doi.org/10.1130/0091-7613(1992)020<0267:RTBAIF>2.3.CO;2)

684 Gardner, T., Webb, J., Pezzia, C., Amborn, T., Tunnell, R., Flanagan, S., Merritts, D.,
685 Marshall, J., Fabel, D., Cupper, M.L., 2009. Episodic intraplate deformation of stable
686 continental margins: evidence from Late Neogene and Quaternary marine terraces, Cape
687 Liptrap, Southeastern Australia. *Quaternary Science Reviews* 28, 39–53.
688 <https://doi.org/10.1016/j.quascirev.2008.10.004>

689 Gray, D.R., Janssen, C., Vapnik, Y., 1999. Deformation character and palaeo-fluid flow
690 across a wrench fault within a Palaeozoic subduction-accretion system: Waratah Fault
691 Zone, southeastern Australia. *Journal of Structural Geology* 21, 191–214.
692 [https://doi.org/10.1016/S0191-8141\(98\)00115-1](https://doi.org/10.1016/S0191-8141(98)00115-1)

693 Gray, D.R., Mortimer, L., 1996. Implications of overprinting deformations and fold
694 interference patterns in the Melbourne Zone, Lachlan Fold Belt. *Australian Journal of*
695 *Earth Sciences* 43, 103–114. <https://doi.org/10.1080/08120099608728240>

696 Gray, D.R., Willman, C.E., 1991. Thrust-related strain gradients and thrusting mechanisms in
697 a chevron-folded sequence, southeastern Australia. *Journal of Structural Geology* 13,
698 691–710. [https://doi.org/10.1016/0191-8141\(91\)90031-D](https://doi.org/10.1016/0191-8141(91)90031-D)

699 Healy, D., Rizzo, R.E., Cornwell, D.G., Farrell, N.J.C., Watkins, H., Timms, N.E., Gomez-

700 Rivas, E., Smith, M., 2017. FracPaQ: A MATLAB™ toolbox for the quantification of
701 fracture patterns. *Journal of Structural Geology* 95, 1–16.
702 <https://doi.org/10.1016/j.jsg.2016.12.003>

703 Heilman, E., Kolawole, F., Atekwana, E.A., Mayle, M., 2019. Controls of Basement Fabric
704 on the Linkage of Rift Segments. *Tectonics*. <https://doi.org/10.1029/2018TC005362>

705 Henza, A.A., Withjack, M.O., Schlische, R.W., 2011. How do the properties of a pre-existing
706 normal-fault population influence fault development during a subsequent phase of
707 extension? *Journal of Structural Geology* 33, 1312–1324.
708 <https://doi.org/10.1016/j.jsg.2011.06.010>

709 Heron, P.J., Peace, A.L., McCaffrey, K.J.W., Welford, J.K., Wilson, R., Hunen, J.,
710 Pysklywec, R.N., 2019. Segmentation of Rifts Through Structural Inheritance: Creation
711 of the Davis Strait. *Tectonics* 38, 2411–2430. <https://doi.org/10.1029/2019TC005578>

712 Hill, K.A., Cooper, G.T., Richardson, M.J., Lavin, C.J., 1994. Structural framework of the
713 Eastern Otway basin: inversion and interaction between two major structural provinces.,
714 *Exploration Geophysics*. <https://doi.org/10.1071/EG994079>

715 Hill, K.C., Hill, K.A., Cooper, G.T., O’Sullivan, A.J., O’Sullivan, P.B., Richardson, M.J.,
716 1995. Inversion around the Bass Basin, SE Australia. *Geological Society, London,*
717 *Special Publications* 88, 525–547. <https://doi.org/10.1144/GSL.SP.1995.088.01.27>

718 Hillis, R.R., Reynolds, S.D., 2000. The Australian Stress Map. *Journal of the Geological*
719 *Society* 157, 915–921. <https://doi.org/10.1144/jgs.157.5.915>

720 Hodge, M., Fagereng, Å., Biggs, J., Mdala, H., 2018. Controls on Early-Rift Geometry: New
721 Perspectives From the Bilila-Mtakataka Fault, Malawi. *Geophysical Research Letters*
722 45, 3896–3905. <https://doi.org/10.1029/2018GL077343>

- 723 Holdgate, G.R., Rodriguez, C., Johnstone, E.M., Wallace, M.W., Gallagher, S.J., 2003. The
724 Gippsland Basin Top Latrobe Unconformity and its expression in other Southeast
725 Australia basins. *The APPEA Journal* 43, 149–173.
- 726 Holdsworth, R.E., Butler, C.A., Roberts, A.M., 1997. The recognition of reactivation during
727 continental deformation. *Journal of the Geological Society* 154, 73–78.
728 <https://doi.org/10.1144/gsjgs.154.1.0073>
- 729 Holdsworth, R.E., Stewart, M., Imber, J., Strachan, R.A., 2001. The structure and rheological
730 evolution of reactivated continental fault zones: a review and case study. *Geological
731 Society, London, Special Publications* 184, 115–137.
732 <https://doi.org/10.1144/GSL.SP.2001.184.01.07>
- 733 Kapp, M.W., Hohenwarter, A., Wurster, S., Yang, B., Pippan, R., 2016. Anisotropic
734 deformation characteristics of an ultrafine- and nanolamellar pearlitic steel. *Acta
735 Materialia* 106, 239–248. <https://doi.org/10.1016/j.actamat.2015.12.037>
- 736 Keetley, J.T., Hill, K.C., Nguyen, C., 2001. Mesoscopic fold and thrust structures at Cape
737 Liptrap, Victoria, Australia; a PNG analogue? In: Hill, K.C., Bernecker, T. (Eds.),
738 Eastern Australasian Basins Symposium. Petroleum Exploration Society of Australia,
739 Melbourne, 25–28.
- 740 Kirkpatrick, J.D., Bezerra, F.H.R., Shipton, Z.K., Do Nascimento, A.F., Pytharouli, S.I.,
741 Lunn, R.J., Soden, A.M., 2013. Scale-dependent influence of pre-existing basement
742 shear zones on rift faulting: a case study from NE Brazil. *Journal of the Geological
743 Society* 170, 237–247. <https://doi.org/10.1144/jgs2012-043>
- 744 Krassay, A.A., Cathro, D.L., Ryan, D.J., 2004. A regional tectonostratigraphic framework for
745 the Otway Basin. In: Boulton, P.J., Johns, D.R., Lang, S.C. (Eds.), Eastern Australasian
746 Basins Symposium II. Petroleum Exploration Society of Australia, Adelaide, 97–116.

747 Lavenu, A.P.C., Lamarche, J., Gallois, A., Gauthier, B.D.M., 2013. Tectonic versus
748 diagenetic origin of fractures in a naturally fractured carbonate reservoir analog (Nerthe
749 anticline, southeastern France). *AAPG Bulletin* 97, 2207–2232.
750 <https://doi.org/10.1306/04041312225>

751 Maerten, L., Gillespie, P., Pollard, D.D., 2002. Effects of local stress perturbation on
752 secondary fault development. *Journal of Structural Geology* 24, 145–153.
753 [https://doi.org/10.1016/S0191-8141\(01\)00054-2](https://doi.org/10.1016/S0191-8141(01)00054-2)

754 Manatschal, G., Lavier, L., Chenin, P., 2015. The role of inheritance in structuring
755 hyperextended rift systems: Some considerations based on observations and numerical
756 modeling. *Gondwana Research* 27, 140–164. <https://doi.org/10.1016/j.gr.2014.08.006>

757 Marchegiani, L., Van Dijk, J.P., Gillespie, P. a, Tondi, E., Cello, G., 2006. Scaling properties
758 of the dimensional and spatial characteristics of fault and fracture systems in the Majella
759 Mountain, central Italy. *Geological Society Special Publication* 261, 113–131.
760 <https://doi.org/10.1144/GSL.SP.2006.261.01.09>

761 Matthews, K.J., Seton, M., Müller, R.D., 2012. A global-scale plate reorganization event at
762 105–100 Ma. *Earth and Planetary Science Letters* 355–356, 283–298.
763 <https://doi.org/10.1016/j.epsl.2012.08.023>

764 McCaffrey, K.J.W., 1997. Controls on reactivation of a major fault zone: the Fair Head–Clew
765 Bay line in Ireland. *Journal of the Geological Society* 154, 129–133.
766 <https://doi.org/10.1144/gsjgs.154.1.0129>

767 McLean, M.A., Morand, V.J., Cayley, R.A., 2010. Gravity and magnetic modelling of crustal
768 structure in central Victoria: what lies under the Melbourne Zone? *Australian Journal of*
769 *Earth Sciences* 57, 153–173. <https://doi.org/10.1080/08120090903416245>

770 Miller, J.M.L., Norvick, M.S., Wilson, C.J.L., 2002. Basement controls on rifting and the
771 associated formation of ocean transform faults - Cretaceous continental extension of the
772 southern margin of Australia. *Tectonophysics* 359, 131–155.
773 [https://doi.org/10.1016/S0040-1951\(02\)00508-5](https://doi.org/10.1016/S0040-1951(02)00508-5)

774 Moore, D.H., Betts, P.G., Hall, M., 2016. Constraining the VanDieland microcontinent at the
775 edge of East Gondwana, Australia. *Tectonophysics* 687, 158–179.
776 <https://doi.org/10.1016/j.tecto.2016.09.009>

777 Morley, C.K., 2010. Stress re-orientation along zones of weak fabrics in rifts: An explanation
778 for pure extension in “oblique” rift segments? *Earth and Planetary Science Letters* 297,
779 667–673. <https://doi.org/10.1016/j.epsl.2010.07.022>

780 Müller, R.D., Seton, M., Zahirovic, S., Williams, S.E., Matthews, K.J., Wright, N.M.,
781 Shephard, G.E., Maloney, K.T., Barnett-Moore, N., Hosseinpour, M., Bower, D.J.,
782 Cannon, J., 2016. Ocean Basin Evolution and Global-Scale Plate Reorganization Events
783 Since Pangea Breakup. *Annual Review of Earth and Planetary Sciences* 44, 107–138.
784 <https://doi.org/10.1146/annurev-earth-060115-012211>

785 Munro, M.A., Blenkinsop, T.G., 2012. MARD-A moving average rose diagram application
786 for the geosciences. *Computers and Geosciences* 49, 112–120.
787 <https://doi.org/10.1016/j.cageo.2012.07.012>

788 Norvick, M.S., Smith, M.A., Power, M.R., 2001. The Plate Tectonic Evolution of Eastern
789 Australasia Guided by the Stratigraphy of the Gippsland Basin. In: Hill, K.C.,
790 Bernecker, T. (Eds.), *Eastern Australasian Basins Symposium*. Petroleum Exploration
791 Society of Australia, Melbourne, 15–23.

792 Norvick, M.S., Smith, M.S., 2001. Mapping the plate tectonic reconstruction of southern and
793 southeastern Australia and implications for petroleum systems. *The APPEA Journal* 41,

794 15–35.

795 O'Brien, G.W., Reeves, C.V., Milligan, P.R., Morse, M.P., Alexander, E.M., Willcox, J.B.,
796 Yunxuan, Z., Finlayson, D.M., Brodie, R.C., 1994. New ideas on the rifting history and
797 structural architecture of the western Otway Basin: evidence from the integration of
798 aeromagnetic, gravity and seismic data. *The APPEA Journal* 34, 529–554.
799 <https://doi.org/https://doi.org/10.1071/AJ93042>

800 Peace, A., McCaffrey, K., Imber, J., van Hunen, J., Hobbs, R., Wilson, R., 2018. The role of
801 pre-existing structures during rifting, continental breakup and transform system
802 development, offshore West Greenland. *Basin Research* 30, 373–394.
803 <https://doi.org/10.1111/bre.12257>

804 Philippon, M., Willingshofer, E., Sokoutis, D., Corti, G., Sani, F., Bonini, M., Cloetingh, S.,
805 2015. Slip re-orientation in oblique rifts. *Geology* 43, 147–150.
806 <https://doi.org/10.1130/G36208.1>

807 Phillips, T.B., Jackson, C.A.L., Bell, R.E., Duffy, O.B., 2018. Oblique reactivation of
808 lithosphere-scale lineaments controls rift physiography - The upper-crustal expression of
809 the Sorgenfrei-Tornquist Zone, offshore southern Norway. *Solid Earth* 9, 403–429.
810 <https://doi.org/10.5194/se-9-403-2018>

811 Phillips, T.B., Jackson, C.A.L., Bell, R.E., Duffy, O.B., Fossen, H., 2016. Reactivation of
812 intrabasement structures during rifting: A case study from offshore southern Norway.
813 *Journal of Structural Geology* 91, 54–73. <https://doi.org/10.1016/j.jsg.2016.08.008>

814 Power, M.R., Hill, K.C., Hoffman, N., 2003. Structural inheritance, stress rotation,
815 overprinting and compressional reactivation in the Gippsland Basin - Tuna 3D seismic
816 dataset. *The APPEA Journal* 43, 197–221.
817 <https://doi.org/https://doi.org/10.1071/AJ02010>

818 Power, M.R., Hill, K.C., Hoffman, N., Bernecker, T., Norvick, M., 2001. The Structural and
819 Tectonic Evolution of the Gippsland Basin: Results from 2D Section Balancing and 3D
820 Structural Modelling. In: Hill, K.C., Bernecker, T. (Eds.), Eastern Australasian Basins
821 Symposium. Petroleum Exploration Society of Australia, Melbourne, 373–384.

822 Reeve, M.T., Bell, R.E., Duffy, O.B., Jackson, C.A.L., Sansom, E., 2015. The growth of non-
823 colinear normal fault systems; What can we learn from 3D seismic reflection data?
824 *Journal of Structural Geology* 70, 141–155. <https://doi.org/10.1016/j.jsg.2014.11.007>

825 Robin, P.Y.F., Jowett, E.C., 1986. Computerized density contouring and statistical evaluation
826 of orientation data using counting circles and continuous weighting functions.
827 *Tectonophysics* 121, 207–223. [https://doi.org/10.1016/0040-1951\(86\)90044-2](https://doi.org/10.1016/0040-1951(86)90044-2)

828 Rohrbaugh, M.B.J., Dunne, W.M., Mauldon, M., 2002. Estimating fracture trace intensity,
829 density, and mean length using circular scan lines and windows. *AAPG Bulletin* 86,
830 2089–2104. <https://doi.org/10.1306/61EEDE0E-173E-11D7-8645000102C1865D>

831 Samsu, A., Cruden, A.R., Hall, M., Micklethwaite, S., Denyszyn, S.W., 2019. The influence
832 of basement faults on local extension directions: Insights from potential field geophysics
833 and field observations. *Basin Research* 31, 782–807. <https://doi.org/10.1111/bre.12344>

834 Schiffer, C., Peace, A., Phethean, J., Gernigon, L., McCaffrey, K., Petersen, K.D., Foulger,
835 G., 2018. The Jan Mayen microplate complex and the Wilson cycle. Geological Society,
836 London, Special Publications 470. <https://doi.org/10.1144/SP470.2>

837 Sibson, R.H., 1985. A note on fault reactivation. *Journal of Structural Geology* 7, 751–754.
838 [https://doi.org/10.1016/0191-8141\(85\)90150-6](https://doi.org/10.1016/0191-8141(85)90150-6)

839 Stubbley, M.P., 1989. Fault and kink-band relationships at Mystery Bay, Australia.
840 *Tectonophysics* 158, 75–92. [https://doi.org/10.1016/0040-1951\(89\)90317-X](https://doi.org/10.1016/0040-1951(89)90317-X)

841 Teasdale, J.P., Pryer, L., Romine, K., Stuart-Smith, P., Etheridge, M., Loutit, T.,
842 Buckingham, A., Shi, Z., Foss, C., Vizy, J., Henley, P., Petrovich, S., Guy-Villon, M.,
843 2004. Australian Southern Margin SEEBASE™ Compilation, April 2004 [WWW
844 Document]. URL <https://data.gov.au/dataset/9131aad8-7d83-4a2b-a678-542e2a1af68a>
845 (accessed 6.26.18).

846 Thiele, S.T., Grose, L., Samsu, A., Micklethwaite, S., Vollgger, S.A., Cruden, A.R., 2017.
847 Rapid, semi-automatic fracture and contact mapping for point clouds, images and
848 geophysical data. *Solid Earth* 8, 1241–1253. <https://doi.org/10.5194/se-8-1241-2017>

849 Thomas, W.A., 2006. Tectonic inheritance at a continental scale. *GSA Today* 16, 4–11.

850 Tommasi, A., Vauchez, A., 2001. Continental rifting parallel to ancient collisional belts: an
851 effect of the mechanical anisotropy of the lithospheric mantle. *Earth and Planetary*
852 *Science Letters* 185, 199–210. [https://doi.org/10.1016/S0012-821X\(00\)00350-2](https://doi.org/10.1016/S0012-821X(00)00350-2)

853 Tveite, H., 2015. The QGIS Line Direction Histogram Plugin [WWW Document]. URL
854 <http://arken.nmbu.no/~havatv/gis/qgisplugins/LineDirectionHistogram/> (accessed
855 7.26.16).

856 Van Noten, K., Van Baelen, H., Sintubin, M., 2012. The complexity of 3D stress-state
857 changes during compressional tectonic inversion at the onset of orogeny. *Geological*
858 *Society Special Publication* 367, 51–69. <https://doi.org/10.1144/SP367.5>

859 Vandenberg, A.H.M., Cayley, R.A., Willman, C.E., Morand, V.J., Seymon, A.R., Osborne,
860 C.R., Taylor, D.H., Haydon, S.J., McLean, M., Quinn, C., Jackson, P., Sandford, A.C.,
861 2006. Walhalla–Woods Point–Tallangalook special map area geological report,
862 Geological Survey of Victoria Report 127. GeoScience Victoria. Department of Primary
863 Industries.

864 VandenBerg, A.H.M., Willman, C.E., Maher, S., Simons, B.A., Cayley, R.A., Taylor, D.H.,
865 Morand, V.J., Moore, D.H., Radojkovic, A., 2000. The Tasman Fold Belt System in
866 Victoria. Geological Survey of Victoria Special Publication 462.

867 Vollgger, S., Cruden, A., 2019. Cape Liptrap orthomosaic.
868 <https://doi.org/https://doi.org/10.26180/5c653193efa25>

869 Vollgger, S.A., Cruden, A.R., 2016. Mapping folds and fractures in basement and cover rocks
870 using UAV photogrammetry, Cape Liptrap and Cape Paterson, Victoria, Australia.
871 *Journal of Structural Geology* 85, 168–187. <https://doi.org/10.1016/j.jsg.2016.02.012>

872 Watkins, H., Bond, C.E., Healy, D., Butler, R.W.H., 2015. Appraisal of fracture sampling
873 methods and a new workflow to characterise heterogeneous fracture networks at
874 outcrop. *Journal of Structural Geology* 72, 67–82.
875 <https://doi.org/10.1016/j.jsg.2015.02.001>

876 Welch, M.J., Souque, C., Davies, R.K., Knipe, R.J., 2014. Using mechanical models to
877 investigate the controls on fracture geometry and distribution in chalk. *Geological*
878 *Society, London, Special Publications* 406, 281–309. <https://doi.org/10.1144/sp406.5>

879 Whipp, P.S., Jackson, C.A.L., Gawthorpe, R.L., Dreyer, T., Quinn, D., 2014. Normal fault
880 array evolution above a reactivated rift fabric; a subsurface example from the northern
881 Horda Platform, Norwegian North Sea. *Basin Research* 26, 523–549.
882 <https://doi.org/10.1111/bre.12050>

883 Willcox, J.B., Colwell, J.B., Constantine, A.E., 1992. New ideas on Gippsland Basin regional
884 tectonics. *Gippsland Basin Symposium 22-23 June 1992. Melbourne*, 93–110.

885 Willcox, J.B., Stagg, H.M.J., 1990. Australia's southern margin: a product of oblique
886 extension. *Tectonophysics* 173, 269–281. [https://doi.org/10.1016/0040-1951\(90\)90223-](https://doi.org/10.1016/0040-1951(90)90223-)

887 U

888 Williams, J.N., Fagereng, Å., Wedmore, L.N.J., Biggs, J., Mphepo, F., Dulanya, Z., Mdala,
889 H., Blenkinsop, T., 2019. How Do Variably Striking Faults Reactivate During Rifting?
890 Insights From Southern Malawi. *Geochemistry, Geophysics, Geosystems*
891 2019GC008219. <https://doi.org/10.1029/2019GC008219>

892 Williams, S.E., Whittaker, J.M., Müller, R.D., 2011. Full-fit, palinspastic reconstruction of
893 the conjugate Australian-Antarctic margins. *Tectonics* 30.
894 <https://doi.org/10.1029/2011TC002912>

895 Wilson, C.J.L., Moore, D.H., Luzin, V., Salvemini, F., 2017. Costerfield antimony-gold
896 deposit, southeast Australia: Coupling between brittle deformation and dissolution-
897 precipitation reactions in the Melbourne Zone. *Ore Geology Reviews* 91, 741–764.
898 <https://doi.org/10.1016/j.oregeorev.2017.08.024>

899 Wilson, J.T., 1966. Did the Atlantic Close and then Re-open? *Nature* 211, 676–681.

900 Wilson, R.W., Holdsworth, R.E., Wild, L.E., McCaffrey, K.J.W., England, R.W., Imber, J.,
901 Strachan, R.A., 2010. Basement-influenced rifting and basin development: a reappraisal
902 of post-Caledonian faulting patterns from the North Coast Transfer Zone, Scotland.
903 Geological Society, London, Special Publications 335, 795–826.
904 <https://doi.org/10.1144/SP335.32>

905 Wilson, R.W., McCaffrey, K.J.W., Holdsworth, R.E., Imber, J., Jones, R.R., Welbon, A.I.F.,
906 Roberts, D., 2006. Complex fault patterns, transtension and structural segmentation of
907 the Lofoten Ridge, Norwegian margin: Using digital mapping to link onshore and
908 offshore geology. *Tectonics* 25, 1–28. <https://doi.org/10.1029/2005TC001895>

909 Wu, H., Pollard, D.D., 1995. An experimental study of the relationship between joint spacing

910 and layer thickness. *Journal of Structural Geology* 17, 887–905.

911 [https://doi.org/10.1016/0191-8141\(94\)00099-L](https://doi.org/10.1016/0191-8141(94)00099-L)

912

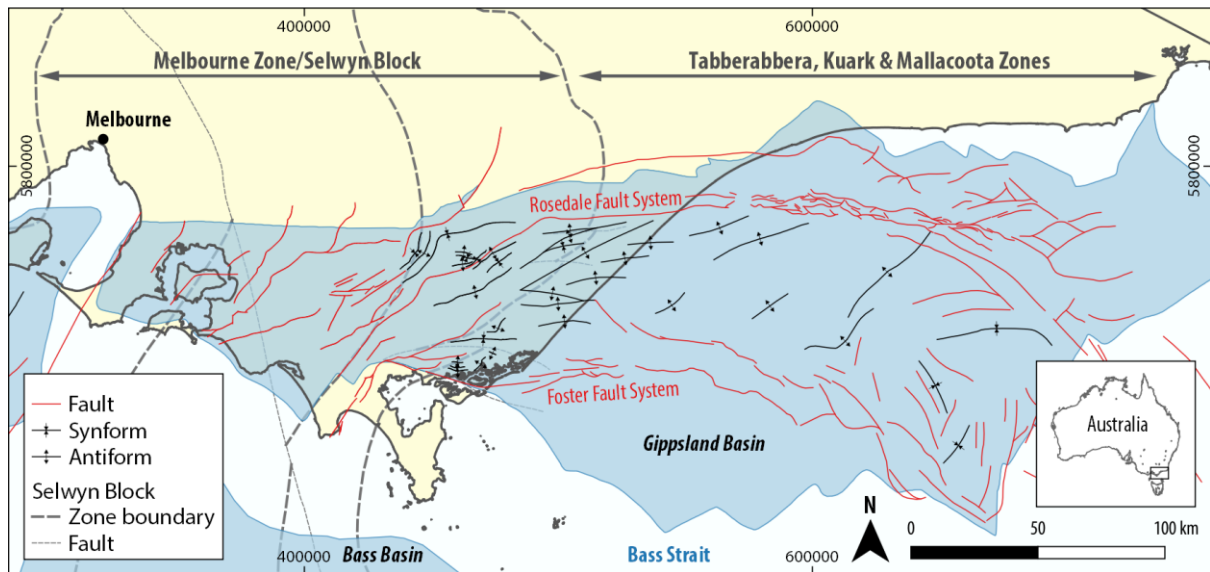
913 **Table 1** Summary of the sequence of ductile and brittle deformation at Shark Stack. The
 914 orientation of the traces of the structures on aerial imagery, the sense of movement along the
 915 horizontal, and the inferred orientation of the maximum horizontal principal stress (σ_H) are
 916 included.

Event	Structures	Trace Azimuth	Sense of Movement	Regime	σ_H Orientation
D1	F1 folds	NNE-SSW 003 - 037°		Contraction	WNW-ESE
D2	F2 kink folds	N-S 355 - 015°	Dextral	Contraction	NNE-SSW
D3	Fractures	ENE-WSW 050 - 075°	Dextral	Extension	ENE-WSW
D4	F4 kinks	NW-SE 310 - 320°	Dextral	Contraction	NNW-SSE
917 D4	Fractures	NNW-SSE 315 - 360°	Sinistral	Contraction	NNW-SSE

918 **Table 2** Fracture trends in Lower Cretaceous Strzelecki Group outcrops. $N_{L \leq 50m}$ = total
 919 number of fracture traces at each locality with a length ≤ 50 m; N_{Trend} = number of fracture
 920 traces belonging to the corresponding trend.

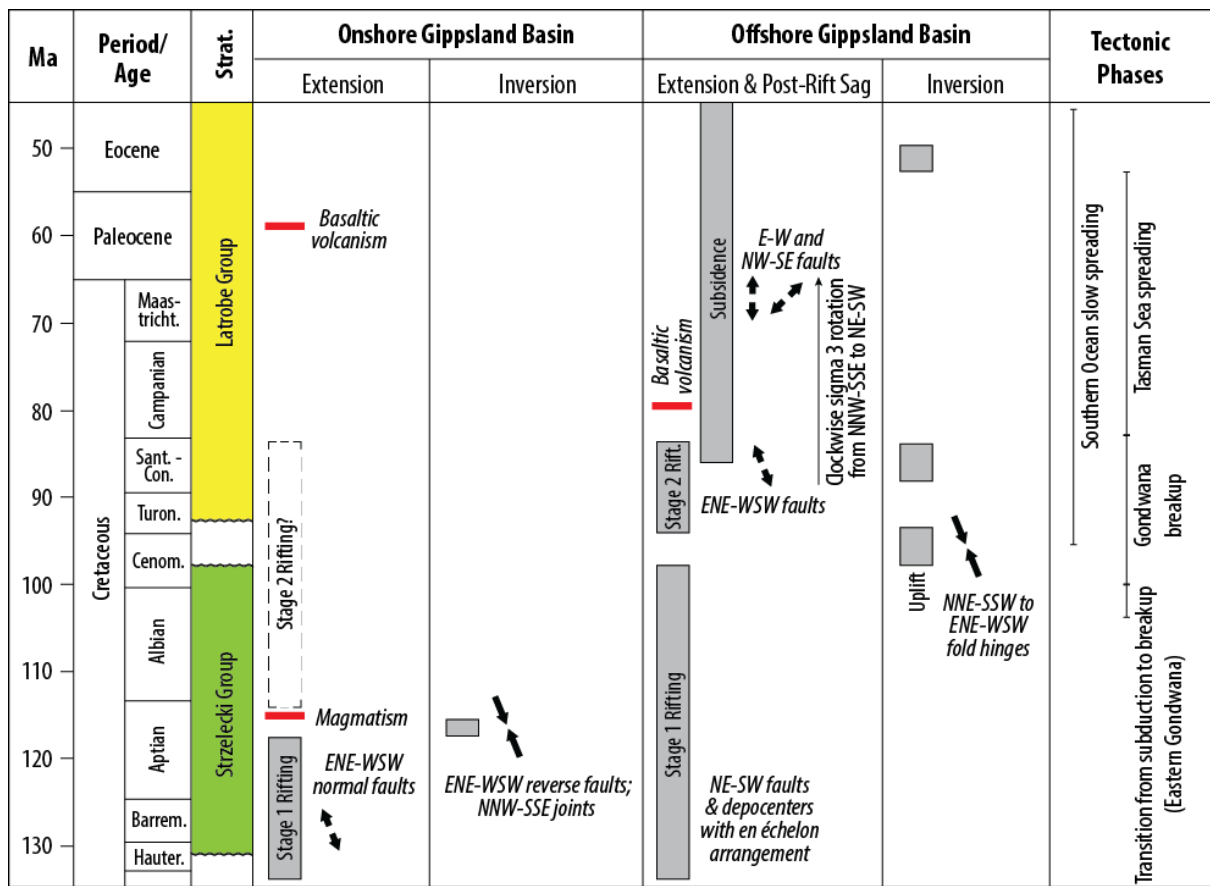
Locality	$N_{L \leq 50m}$	Trend Azimuth		N_{Trend}
Harmers Haven North	1308	NNW-SSE	335 - 350°	267
		WNW-ESE	280 - 295°	246
		E-W	080 - 100°	259
Harmers Haven South	2497	NNW-SSE	325 - 345°	1055
Eagles Nest	1443	NNW-SSE	325 - 345°	404
		ENE-WSW	065 - 080°	180
		E-W	080 - 095°	188
The Caves - Flat Rocks	1591	NNW-SSE	320 - 345°	522
		ENE-WSW	065 - 085°	239
		NNE-SSW	010 - 020°	126
Inverloch	378	NW-SE to NNW-SSE	315 - 345°	141
		E-W	085 - 090°	27
		WNW-ESE to NW-SE	290 - 315°	86

921



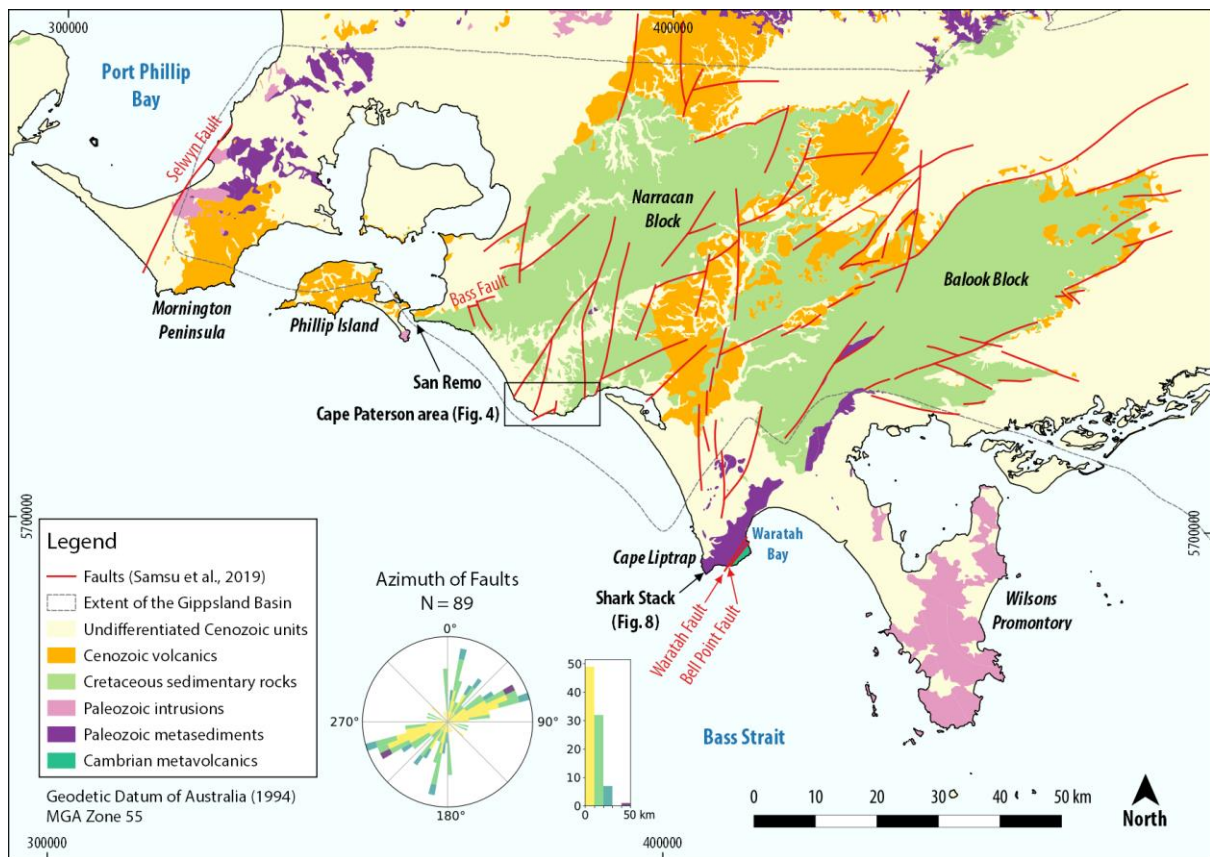
922

923 **Figure 1** Location and major structures of the Cretaceous Gippsland Basin and the nearby
 924 Bass Basin (shaded in blue). Areas that are underlain by the Selwyn Block (Moore et al.,
 925 2016) and Melbourne Zone are shaded in grey. Faults and folds in the Gippsland Basin are
 926 modified after Constantine (2001) and Power et al. (2001). From west to east, the trends of
 927 fault traces change from NE-SW and ENE-WSW (western onshore Gippsland Basin), to E-W
 928 and NW-SE (eastern onshore and offshore Gippsland Basin); this transition defines, in part,
 929 the eastern margin of the Selwyn Block (Cayley et al., 2002). The coordinate reference
 930 system is GDA94 / MGA zone 55.



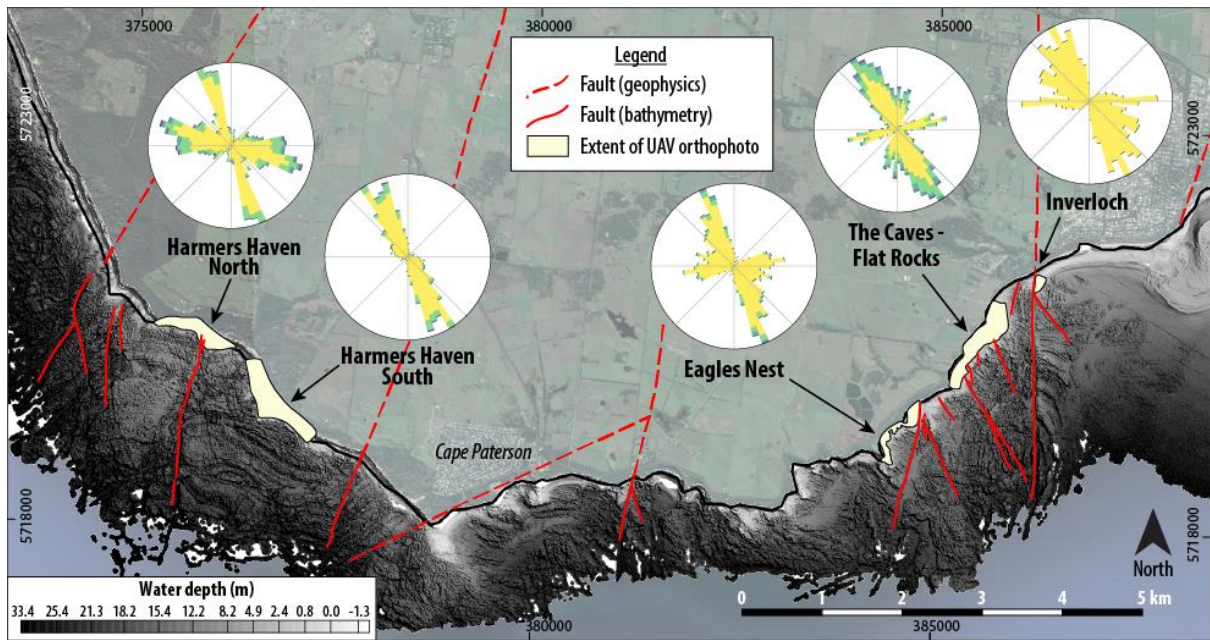
931

932 **Figure 2** Summary of the deformation history in the Gippsland Basin and associated tectonic
 933 events. Deformation events in the offshore Gippsland Basin and basaltic volcanism are
 934 derived from seismic reflection studies (Norvick et al., 2001; Power et al., 2003). Early
 935 Cretaceous deformation and magmatism in the onshore Gippsland Basin are derived from
 936 field studies and regional potential field geophysics (Samsu et al., 2019). Arrows indicate
 937 local extension and shortening directions inferred from fault orientations.



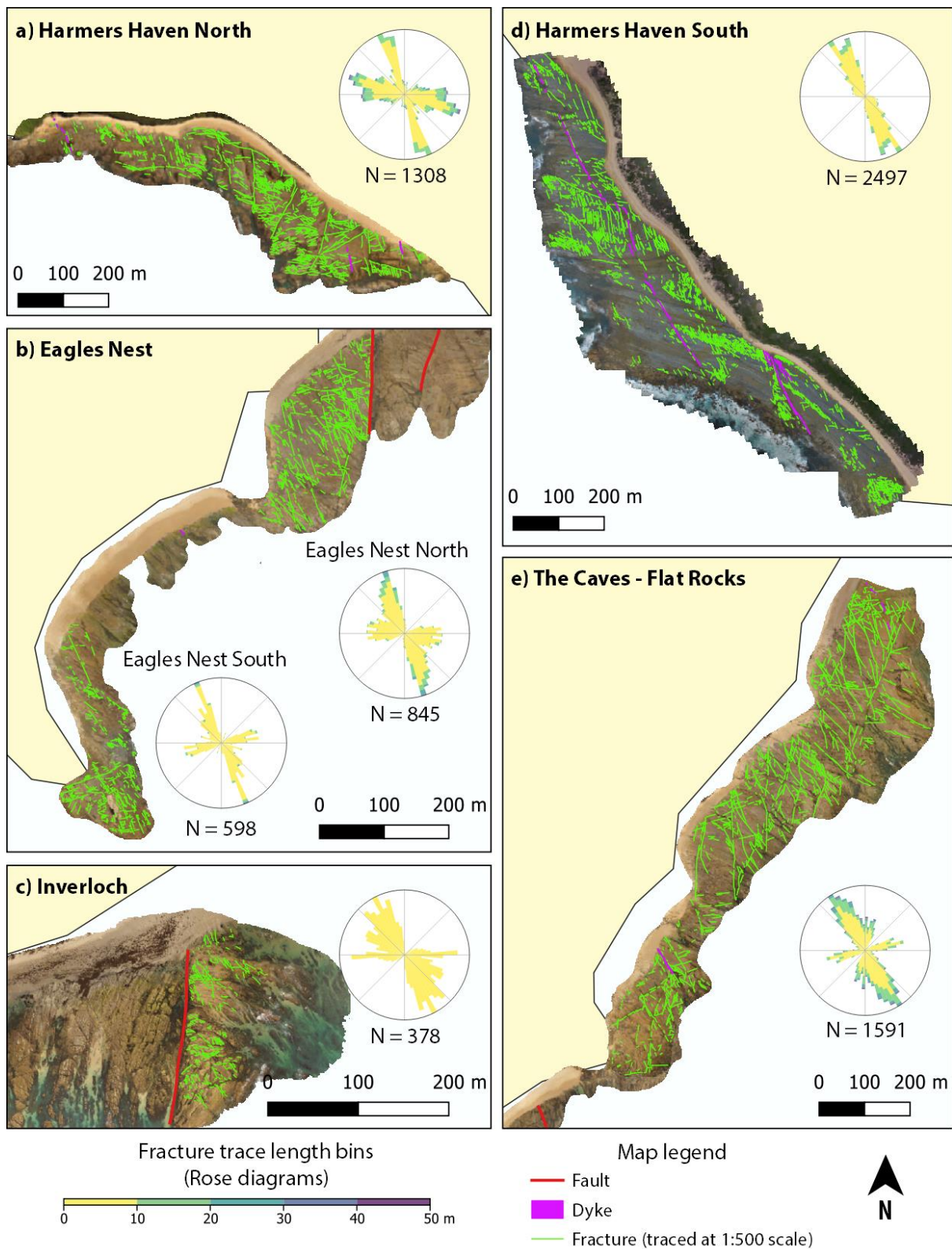
938

939 **Figure 3** Map of basin-scale (>1 km-scale) faults interpreted from magnetic and gravity data
 940 (modified after Samsu et al., 2019). The rose diagram of fault traces was created using the
 941 GeoTrace plugin (Thiele et al., 2017) in QGIS and is coloured by fault length. Colours on the
 942 rose diagram correlate with fault length bins shown on the length histogram. The coordinate
 943 reference system is GDA94 / MGA zone 55.



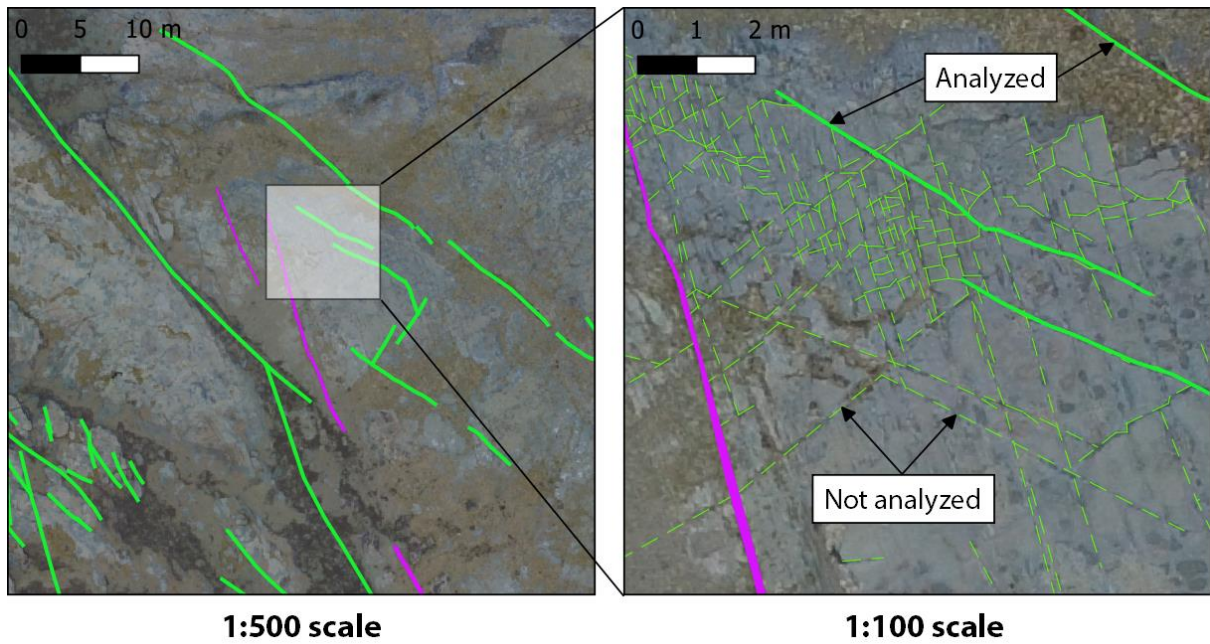
944

945 **Figure 4** Map of the UAV photogrammetry survey areas, where outcrop-scale fractures in the
 946 Lower Cretaceous Strzelecki Group were traced, overlain on a greyscale image of near-shore
 947 bathymetry (modified after Samsu et al., 2019). The frequency of the orientations of fracture
 948 traces from each area is visualised as length-coloured rose diagrams. Colours correspond to
 949 fracture length, subdivided into 10 m bins (see Fig. 5 for colour ramp of length bins). See Fig.
 950 3 for location of map.



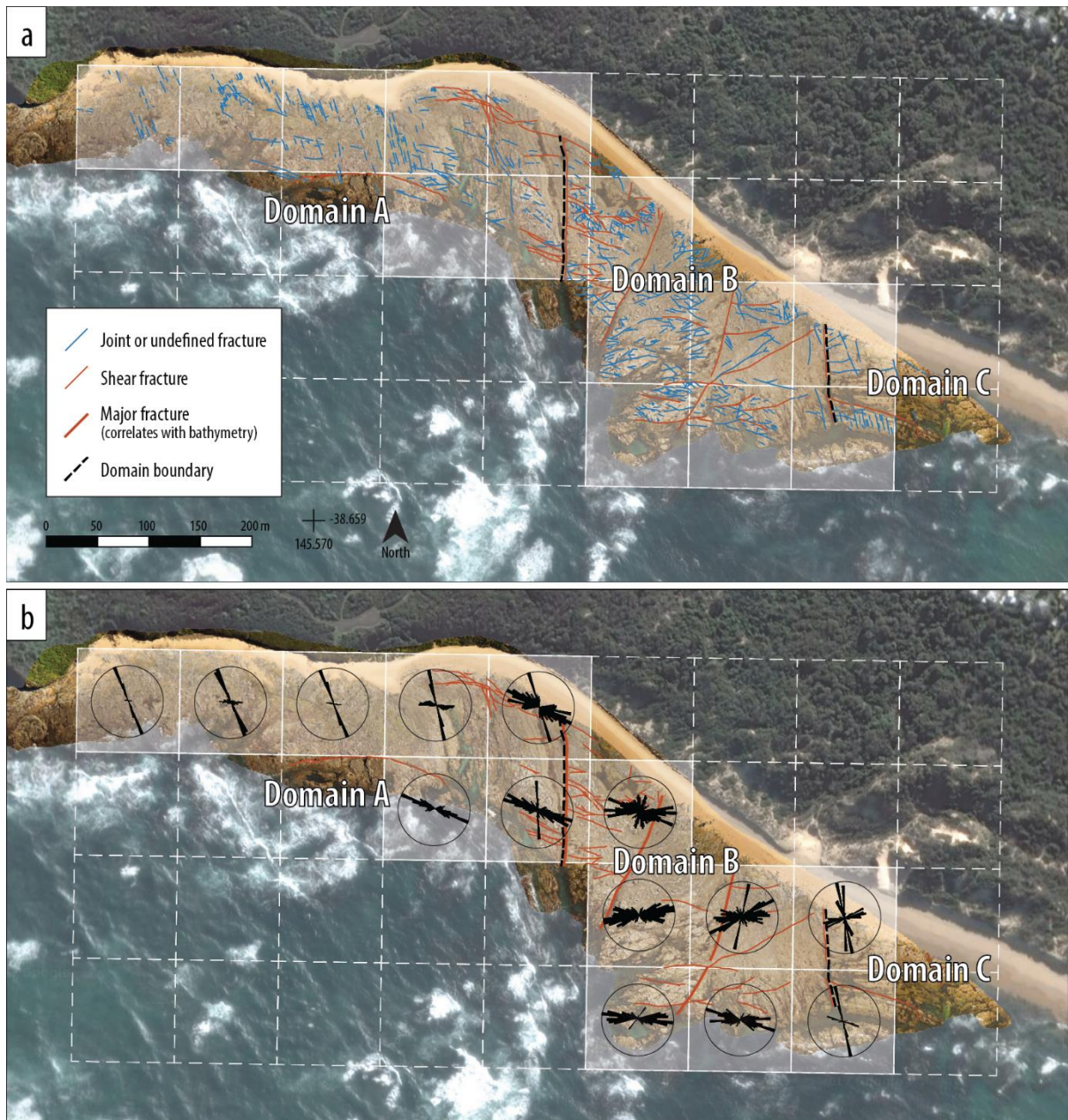
951

952 **Figure 5** Fracture trace maps and rose diagrams, representing fractures <50 m in length, for
 953 the five studied outcrops (see Fig. 4 for locations). Fracture traces (interpreted at a scale of
 954 1:500) are overlain on UAV orthophotos. Colours on the rose diagram correspond to fracture
 955 length, subdivided into 10 m bins.



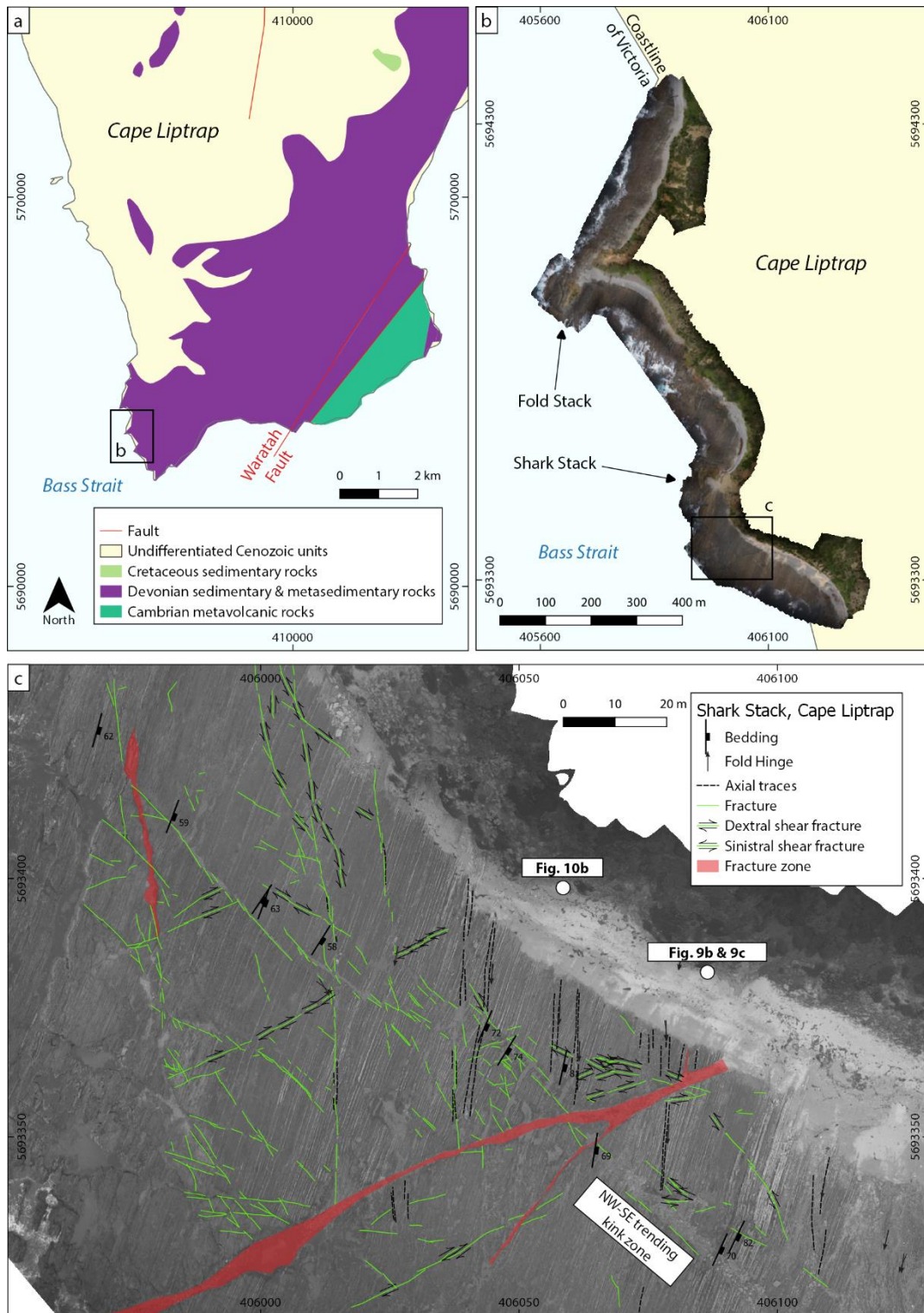
956

957 **Figure 6** Fracture traces (green) interpreted from UAV orthophotos at 1:500 and 1:100 zoom
 958 levels. Fractures that can be seen at the 1:500 scale (thick, continuous lines) were included in
 959 the analyses of fracture orientations, so that we only compare fractures between outcrops that
 960 are observable at the same scale. Purple traces represent mafic dykes.



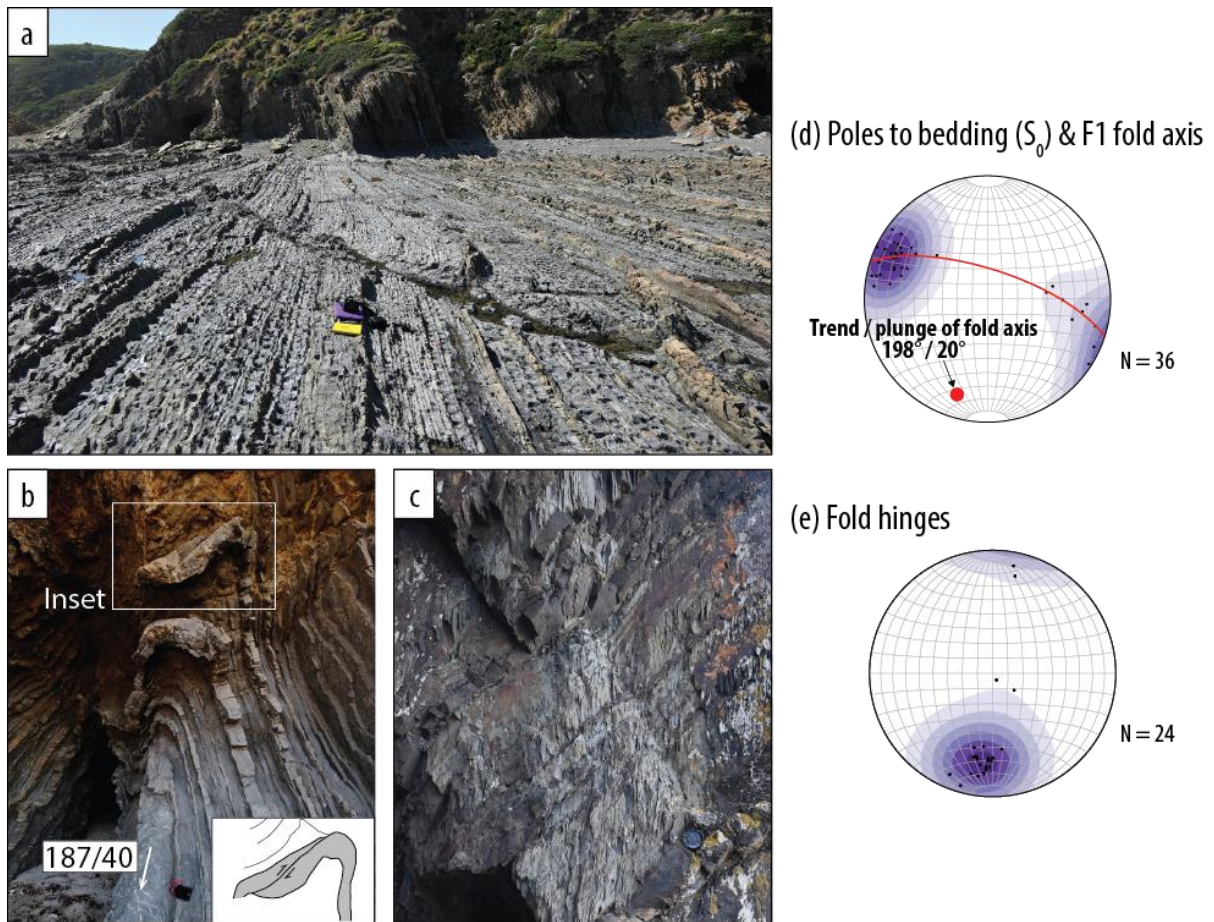
961

962 **Figure 7** (a) Fracture trace map of the Harmers Haven North locality. The basemap is a high-
 963 resolution (3 cm/pixel) UAV orthophoto. A grid made up of 100 m x 100 m tiles is overlain
 964 on the orthophoto. (b) Length-weighted rose diagrams of fracture trace orientations calculated
 965 for each tile using the Line Direction Histogram plugin (Tveite, 2015) in QGIS. The
 966 background is a satellite image (source: Google Earth, 38.657362° and 145.572051°, May 14,
 967 2016, accessed July 30, 2017).



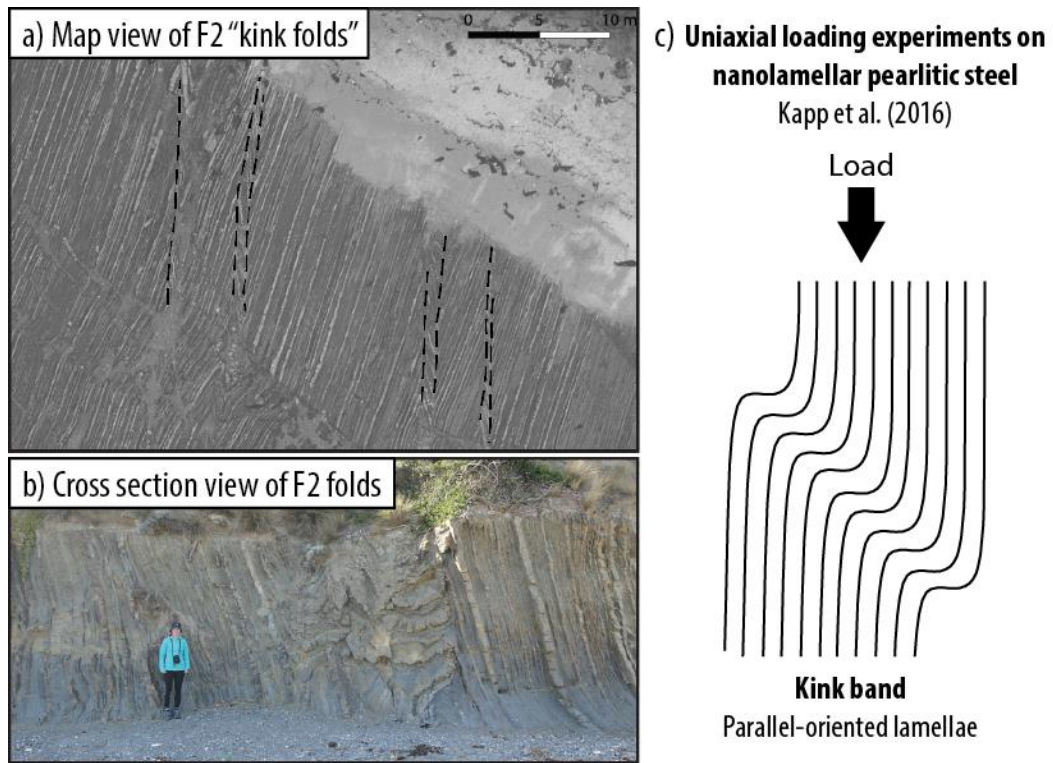
968

969 **Figure 8** (a) Location of Shark Stack study area at the southwestern end of Cape Liptrap (see
 970 Fig. 3 for location), where a UAV orthophoto (b; 2 cm/pixel) was used as a basemap for
 971 structural mapping in the field. Structures at the Fold Stack locality have been described in
 972 detail in Vollgger and Cruden (2016). (c) Map of fractures, axial traces of folds, and
 973 structural measurements at Shark Stack. All of the fractures that are visible at a 1:500 scale
 974 are shown.



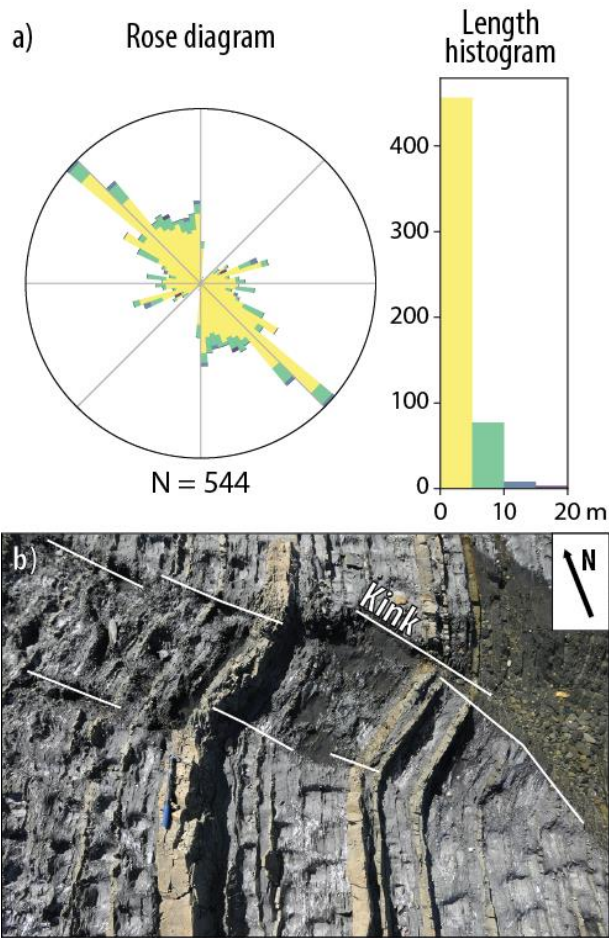
975

976 **Figure 9** Structures at Shark Stack, Cape Liptrap: (a) Photograph of steeply dipping,
 977 alternating beds of sandstone and mudstone cropping out on a horizontal wavecut platform
 978 and along vertical cliff faces. These rocks form the Devonian basement underlying the
 979 onshore Gippsland Basin. (b) Photograph of disharmonic F2 folds exposed in a cliff face. The
 980 inset shows a fold accommodation fault offsetting a sandstone bed in a reverse sense near the
 981 fold hinge. The arrow indicates the measured orientation of the hinge line. (c) Photograph of
 982 axial planar cleavage and parasitic folds on the limb of an F1 fold. (d) Plot of poles to
 983 bedding measurements and the axis of a first-order F1 fold calculated from bedding
 984 measurements. (e) Plot of measured fold hinges; F2 kink fold hinges associated with a D2
 985 contractional event plunge shallowly to the south. Subvertical fold hinges may be associated
 986 with slump folds and are therefore non-tectonic in nature. Pole orientations were contoured
 987 using the Exponential Kamb method at intervals of 3σ .



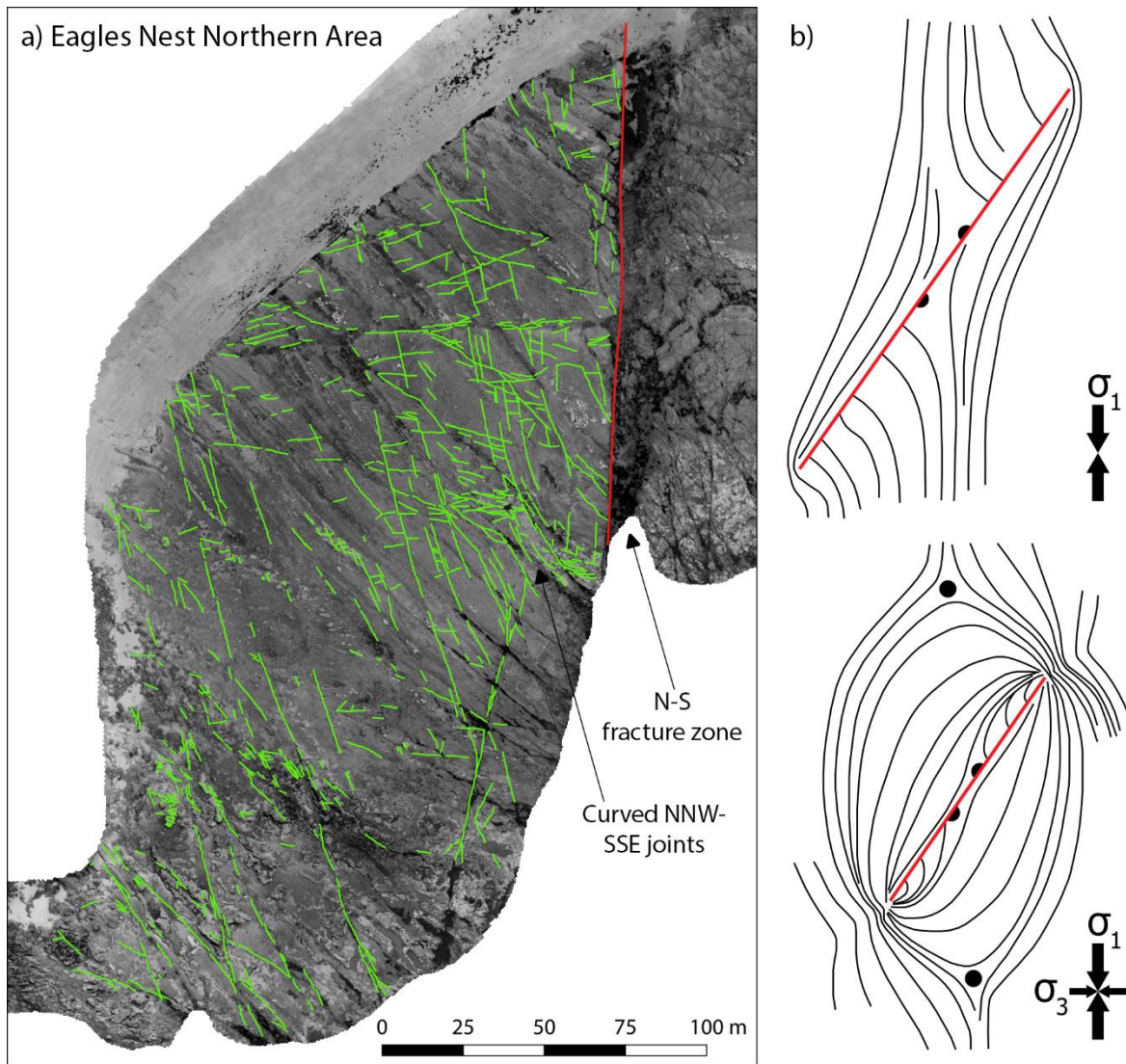
988

989 **Figure 10** N-S trending zones of kinking in the wavecut platform (a) and cliff (b). Dashed
 990 lines represent axial traces of F2 kink folds. Kink folds at Shark Stack are analogous to kink
 991 bands in nanolamellar pearlitic steel (c) (modified after Kapp et al., 2016).



992

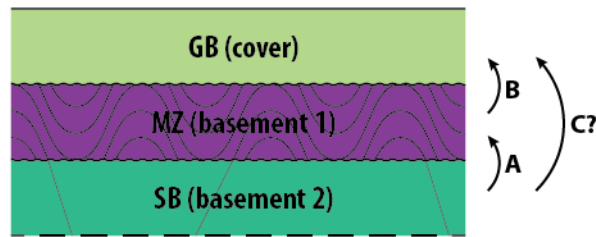
993 **Figure 11** (a) Length-coloured rose diagram of outcrop-scale fractures at Shark Stack. (b)
 994 The NW-SE trending peak represents a large population of kinks that make up the NW-SE
 995 trending F3 kink bands. The length-coloured rose diagram allows us to assign fractures of
 996 different length ranges to certain orientation trends. NW-SE kinks are <10 m in length, most
 997 of them being shorter than 5 m. Fractures that are longer than 10 m trend NNW-SSE and
 998 ENE-WSW.



999

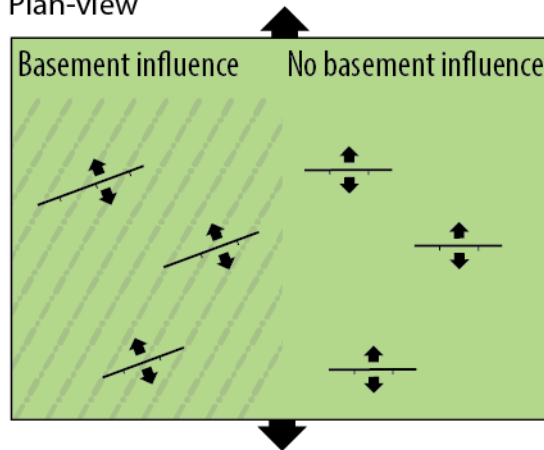
1000 **Figure 12** (a) Fracture traces at the northern part of the Eagles Nest locality, overlain on a
 1001 high-resolution (3.2 cm/pixel) UAV orthophoto (See Fig. 4 for location). Veering of NNW-
 1002 SSE trending joints in the vicinity of the large N-S trending fault is observed, which may be
 1003 caused by perturbed stress trajectories around the larger fault. A similar phenomenon has
 1004 been observed in photoelastic experiments of uniaxial and biaxial loading on analogue
 1005 materials (b; modified from de Jossineau et al., 2003). The red line represents a pre-existing
 1006 fault, and black circles and half circles are isotropic points.

a) Cross-section



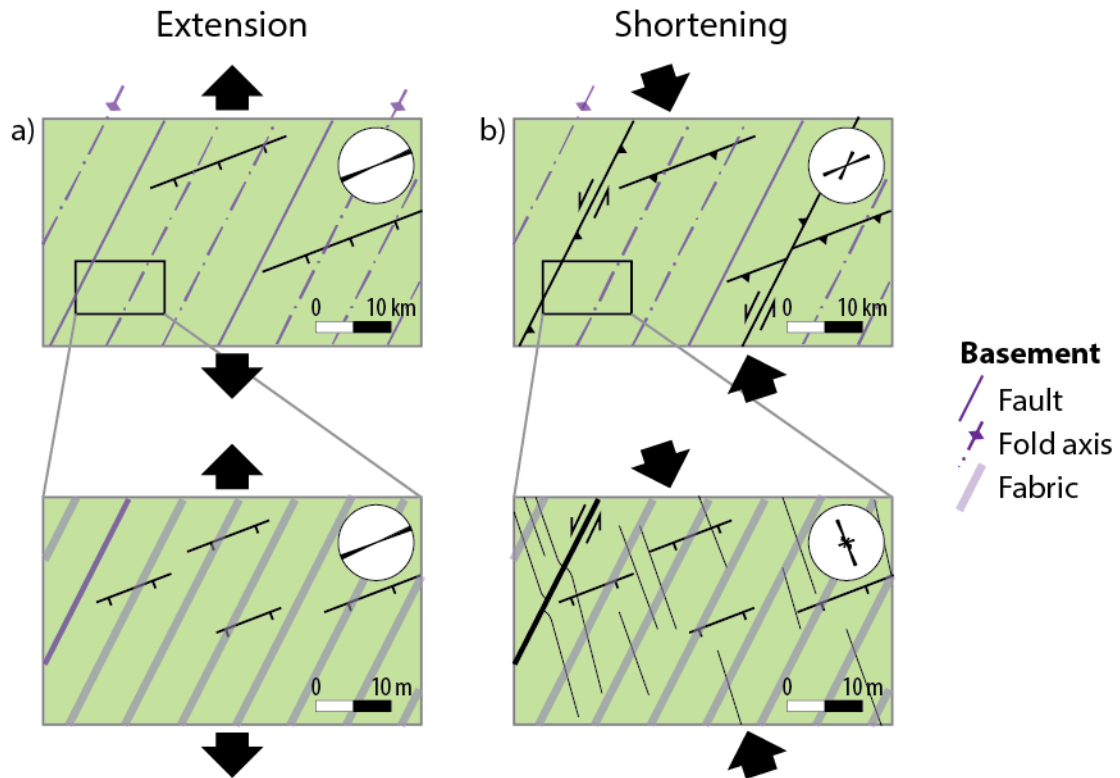
- A. Reactivation of SB faults influenced MZ faults
- B. MZ faults and fabric influenced GB faults
- C. Anomalously strong SB influenced GB faults?

b) Plan-view



1007

1008 **Figure 13** (a) Schematic cross section demonstrating the influence of different basement
 1009 units on overlying units. Devonian faulting in the Melbourne Zone could have been
 1010 controlled by the reactivation of pre-existing Cambrian faults in the Selwyn Block (A). The
 1011 complex array of Early Cretaceous normal faults could have resulted from local stress re-
 1012 orientation above Devonian faults and penetrative fabrics in the Melbourne Zone (B). It
 1013 remains unclear how the relatively high strength of the Selwyn Block, juxtaposed against the
 1014 weaker surrounding lower crust, could have affected Early Cretaceous rifting (C). GB =
 1015 Gippsland Basin; MZ = Melbourne Zone; SB = Selwyn Block. (b) Schematic map-view
 1016 illustration of normal fault orientations: They are oblique to the regional extension direction
 1017 above an anisotropic basement, but they are orthogonal to regional extension where the
 1018 basement is less influential.



1019

1020 **Figure 14** Plan-view schematic illustration of fracture traces in the cover – associated with
 1021 Early Cretaceous extension (a) followed by shortening (b) – and their trends. The purple lines
 1022 represent structures in the underlying Melbourne Zone basement. Extension-related fractures
 1023 show the same ENE-WSW trend at basin scale (>1 km) and outcrop scale (meters-scale).
 1024 During subsequent shortening, pre-existing basement structures and rift-related ENE-WW
 1025 trending fractures are reactivated, so that new fractures are localised above or near reactivated
 1026 structures at the basin scale. At outcrop scale, new sub-vertical joints formed parallel to the
 1027 direction of regional compression, though some joints veer towards larger, pre-existing faults.